A HYBRID SPECTRAL-COMPACT SCHEME FOR TURBULENCE-RESOLVING SIMULATIONS OF FINE SEDIMENT TRANSPORT IN THE BOTTOM BOUNDARY LAYER

BY

XIAO YU AND TIAN-JIAN HSU
CENTER FOR APPLIED COASTAL RESEARCH
UNIVERSITY OF DELAWARE

S. BALACHANDAR
MECHANICAL & AEROSPACE ENGINEERING
UNIVERSITY OF FLORIDA

RESEARCH REPORT NO. CACR-12-07
DECEMBER 2012

CENTER FOR APPLIED COASTAL RESEARCH

Ocean Engineering Laboratory
University of Delaware
Newark, Delaware 19716

Acknowledgements

This study is supported by U.S. Office of Naval Research (N00014-11-1-0270) and National Science Foundation (OCE-1130217) to University of Delaware and National Science Foundation (OCE-1131016) to University of Florida. Simulations presented in this paper are carried out on CHIMERA at the University of Delaware with funding supported by the National Science Foundation (CNS-0958512) and the Extreme Science and Engineering Discovery Environment (XSEDE), which is supported by National Science Foundation grant number (TG-OCE100015).

Abstract

A hybrid spectral-compact finite difference scheme for turbulent-resolving simulation of fine sediment transport in bottom boundary layer is presented. The numerical model extends an earlier pseudo-spectral model for direct numerical simulation (DNS) of turbulent flow with a sixth-order compact finite difference scheme in the wall-normal direction on Chebyshev grid points. The compact finite difference scheme allows easy implementation of flow-dependent properties (e.g., viscosity, diffusivity and settling velocity) and more flexible boundary conditions while still maintain spectral-like accuracy. The numerical model is validated with analytical solutions of flow velocity and particle concentration of two simple Newtonian rheology closures in laminar channel flow as well as prior laboratory and DNS data of turbulent channel flow. Several numerical simulations were carried out in a turbulent channel flow setting to investigate the interplay between two turbulence modulation mechanisms induced by the presence of sediment, namely the sediment-induced density stratification and the effects of rheological stress. We demonstrate that at the given Reynolds number, Richardson number, and nondimensional settling velocity considered here, the flow remains turbulent but sediment-induced density stratification already cause noticeable drag reduction. By further introducing a Newtonian rheological stress into the system, onset of laminarization is observed due to the enhanced viscosity.

Contents

List of Figures

List of Tables

1 Introduction

Understanding the deposition, resuspension and transport of fine sediment in fluvial, estuarine and coastal environments is vital to the prediction of a variety of water resource problems. For example, to maintain the navigation of waterways, dredging is routinely carried out in numerous inlets and estuaries throughout the world. Moreover, the dispersal and the fate of these dredged sediments, sometimes contaminated, become another critical concern. Through flocculation, fine sediment transport becomes the vehicle for the transport of carbon, nutrient and pollutant [*Santschi et al.*(2005)]. Hence, the timing and amount of fine sediments resuspended by tidal currents and waves from the benthic zone are critical to the geo-chemistry and biological response of an ecosystem.

There are several main challenges in modeling fine sediment transport in the bottom boundary layer due to the co-existence and the strong coupling of several mechanisms. The presence of fine sediments can attenuate flow turbulence, enhances mean flow (i.e., drag reduction), and in turn suppresses sediment suspension. When sediment concentration becomes large, inter-particle (or inter-floc) interactions give rise to rheological stress that can be parameterized with an enhanced viscosity (i.e., Newtonian [*Einstein*(1906), *Krieger*(1972), *Krieger and Dougherty*(1959)]) or a shear thinning [*Stickel and Powell*(2005)] and a yield behavior [*Kessel and Kranenburg*(1996), *Liu and Mei*(1990)]). It is well-established from experimental and field observations that transport of fine sediment (i.e., mud) often experiences transition from turbulent to laminar condition [*Kessel and Kranenburg*(1996), *Sahin et al.*(2012), *Traykovski*(2010)]. Such transition has critical implications to large-scale fluid mud transport and hydrodynamic dissipation. For instance, Winterwerp (2001) demonstrated that the transition between turbulent and laminar condition in a mud-laden tidal boundary layer is directly associated with the sediment carrying capacity. Under dilute flow assumptions without the consideration of rheological stress, the laminarization can be attributed to

sediment-induced stable density stratification [*Winterwerp*(2001), *Cantero et al.*(2009), *Cantero et al.*(2012), *Ozdemire et al.*(2010)]. On the other hand, Kessel and Kranenburg (1996) model the observed turbulent-laminar transition of fluid mud on a sloping bed solely based on rheological stress. Essentially, they show that through both enhanced effective viscosity and yield stress [*Liu and Mei*(1990)], rheological stress can reduce the effective Reynolds number and trigger laminarization. In general, both turbulence modulation and rheological stress co-exist in fine sediment transport. We are motivated to develop a turbulence-resolving simulation model for fine sediment transport that is capable of incorporating rheological stress and turbulence modulation in order to investigate the inter-play between these two mechanisms in determining the resulting turbulent-laminar flow transition.

To investigate the transition between laminar and turbulent conditions due to turbulence modulation and rheological stress, a turbulence-resolving simulation approach is adopted in the present study. Because our primary goal is to resolve a wide range of turbulent length scales (at lower Reynolds number, all the scales of turbulence are resolved), a 3D numerical scheme with high accuracy is required. Pseudo-spectral methods are widely used in direct numerical simulations of turbulent flow [*Kim et al.*(1987), *Moser and Moin*(1987), *Spalart*(1988)] due to its high accuracy. By using information from the whole computational domain to calculate the derivatives, the pseudo-spectral method converges exponentially towards the exact solution with high accuracy for a wide range of scales. Pseudo-spectral method is, however, not flexible in terms of boundary conditions[*Boyd*(2001), *Gottlieb and Orszag*(1987), *Canuto et al.*(2011)]. For sediment transport applications where the viscosity, diffusivity and settling velocity are generally flow-dependent variables, the applicability of the pseudo-spectral scheme is limited.

On the other hand, explicit finite difference and finite volume methods are the most

widely used numerical schemes due to its robustness in handling complex boundary conditions, flow properties and complicated geometries. However, these schemes only use neighboring points provided by the given stencil size, and converge slowly to the exact solution. To achieve the same accuracy as the pseudo-spectral method in a turbulence-resolving simulation, grid refinement is required. With its spectral-like resolution, reasonable computational cost and its robustness in terms of boundary conditions, compact finite difference methods [*Lele*(1992)] are becoming popular in CFD community [*Shah et al.*(2010), *Hokpunna and Manhart*(2010), *Boersma*(2011), *Pereira et al.*(2001), *Shukla et al.*(2007)]. The first-order and higher-order derivatives are calculated implicitly with the information from all grid points of the computational domain for compact finite difference schemes. Compared to explicit finite difference schemes, compact finite difference schemes provide significantly higher accuracy with the same stencil size [*Lele*(1992)]. This point will be illustrated in more details in Section 3.6.

The purpose of this report is to present a 3D turbulence-resolving numerical simulation model for fine sediment transport in the bottom boundary layer based on a hybrid spectral and compact finite difference scheme. Model formulation for fine sediment transport following equilibrium Eulerian approximation of Balachandar and Eaton (2010), appropriate for small Stokes number, is briefly discussed in Section 2. The numerical scheme of the present model, which extends from an earlier pseudo-spectral scheme of Cortese and Balachandar (1995) with the implementation of compact difference scheme in the vertical direction is discussed in Section 3. Section 4 presents model validations and applications. Specifically, we present a preliminary investigation in Section 4.2 on how Newtonian rheology with an enhanced viscosity can trigger laminarization of fine sediment in a turbulent boundary layer in conjunction with sediment-induced density stratification. Conclusion and future works are summarized in Section 5.

2 Model Formulation

In this study, we consider fine sediment transport in a turbulent flow with the Stokes number ($St = \tau_p/\tau_f$ with τ_p the particle response time and τ_f the fluid time scale) smaller than unity. Ferry and Balachandar (2001) demonstrated that for particles with small Stokes number ($St << 1$), the equilibrium approximation can be adopted where sediment phase velocity can be given explicitly as the sum of the fluid phase velocity, the settling velocity of sediment particle, and an asymptotic expansion of the Stokes number *St* (see also Ferry and Balachandar (2002) and a more recent review by Balachandar and Eaton (2010))

$$\tilde{\mathbf{v}} = \tilde{\mathbf{u}} + \tilde{\mathbf{W}}_s + O(St) \tag{1}$$

$\tilde{\mathbf{u}}$ is the fluid phase velocity, $\tilde{\mathbf{v}}$ is the sediment phase velocity and $\tilde{\mathbf{W}}_s$ is the settling velocity of particles. In this report, the variables with $\tilde{}$ represents dimensional flow variables. The key advantage of the equilibrium approximation is that the particle phase velocity can be explicitly calculated via the algebraic relationship shown in equation (1) without the need to solve the full momentum equations of the particle phase. As shown by Cantero et al. (2009), by substituting equation (1) into the standard Eulerian-Eulerian two-phase equations for fluid and particle phase and making the Bousinessq approximation, the resulting governing equations for fine sediment transport become

$$\tilde{\nabla} \cdot \tilde{\mathbf{u}} = 0 \tag{2}$$

$$\frac{\partial \tilde{\mathbf{u}}}{\partial \tilde{t}} + \tilde{\mathbf{u}} \cdot \tilde{\nabla}\tilde{\mathbf{u}} = -\frac{1}{\rho}\tilde{\nabla}\tilde{p} + \tilde{\nabla} \cdot [\nu(\tilde{\nabla}\tilde{\mathbf{u}} + \tilde{\nabla}\tilde{\mathbf{u}}^T)] + g\tilde{\phi}\mathbf{e_3} \tag{3}$$

$$\frac{\partial \tilde{\phi}}{\partial \tilde{t}} + \tilde{\nabla} \cdot (\tilde{\mathbf{v}}\tilde{\phi}) = \tilde{\nabla} \cdot (\kappa\tilde{\nabla}\tilde{\phi}) \tag{4}$$

where ν is the effective kinematic viscosity of the fluid, and κ is the diffusion coefficient of the sediment phase. In this set of simplified governing equations, which are appropriate for small Stokes number, the continuity and momentum equations of the carrier

fluid phase are similar to the Navier-Stokes equations. The only coupling term between the particle phase and the carrier fluid is the particle-induced density stratification (see the last term in equation (3)). The sediment phase is calculated by the mass balance with particle phase velocity computed by equation 1. In Section 5, we will justify that the fine sediment transport problem investigated in this study satisfies the small Stokes number assumption.

There have been many studies on the effective viscosity of fluid with the presence of (sediment) particles. These rheology models consider the viscosity as a function of the sediment concentration $\tilde{\phi}$ and the shear rate[*Stickel and Powell*(2005)]. Since the main purpose of this study is to introduce the numerical model and carry out preliminary investigation on the interplay between rheology and turbulence closure, we consider the effective viscosity to be only a function of sediment concentration, i.e. Newtonian rheology with $\nu = \nu_0 \tilde{f}(\tilde{\phi})$, where ν_0 is the kinematic viscosity of the clear fluid. Under the action of shear, the settled particles can be resuspended in turbulent flow. This shear-induced dispersion is very important in mixing sediment particles, and the shear-induced sediment phase diffusion coefficient has also been widely studied [*Schaflinger et al.*(1990), *Acrivos et al.*(1993), *Leighton and Acrivos*(1986)]. The diffusivity of sediment phase is given as a function of $\tilde{\phi}$ only, $\kappa = \kappa_0 \tilde{h}(\tilde{\phi})$.
If we choose the characteristic length scale L, the characteristic velocity scale U and the volume averaged sediment concentration $\Phi = \int_V \tilde{\phi}(\tilde{x}, \tilde{y}, \tilde{z}) d\tilde{\mathbf{V}}/V$, define

$$\mathbf{x} = \frac{\tilde{\mathbf{x}}}{L}, \quad t = \frac{\tilde{t}}{L/U}, \quad \mathbf{u} = \frac{\tilde{\mathbf{u}}}{U}, \quad \mathbf{v} = \frac{\tilde{\mathbf{v}}}{U}, \quad p = \frac{\tilde{p}}{\rho U^2} \quad \phi = \frac{\tilde{\phi}}{\Phi} \tag{5}$$

above governing equations can be non-dimensionalized

$$\nabla \mathbf{u} = 0 \tag{6}$$

$$\frac{\partial \mathbf{u}}{\partial t} + \mathbf{u} \cdot \nabla \mathbf{u} = -\nabla p + \frac{1}{Re} \nabla \cdot [f(\phi)(\nabla \mathbf{u} + \nabla \mathbf{u}^T)] + Ri \phi \mathbf{e_3} \tag{7}$$

$$\frac{\partial \phi}{\partial t} + \nabla \cdot (\mathbf{v}\phi) = \frac{1}{ReSc} \nabla \cdot (h(\phi) \nabla \phi) \tag{8}$$

$$\mathbf{v} = \mathbf{u} + \mathbf{W}_s + O(St) \tag{9}$$

where the non-dimensional groups are defined as

$$Re = \frac{UL}{\nu_0}, \qquad Ri = \frac{gL(\gamma - 1)\Phi}{U^2}, \qquad Sc = \frac{\nu_0}{\kappa_0}, \quad \mathbf{W}_s = \frac{\tilde{\mathbf{W}}_s}{U} \tag{10}$$

where $\gamma = \rho^s / \rho^f$ is the specific gravity of sediment particles. The forms of $f(\phi)$ and $h(\phi)$ depend on the rheological model adopted. In this study, we adopt simple Newtonian rheology closures that only involve $f(\phi)$ and the diffusivity of the sediment phase is set to be a constant $\kappa = \kappa_0$ (i.e., $h(\phi) = 1$).

3 Numerical method

The mathematical formulation presented in the previous section is rather general for fine sediment transport modeling. In this study, we utilize this formulation to study fine sediment transport in the bottom boundary layer. A detailed description of the numerical schemes along with boundary conditions are presented in this section. We modified the spectral scheme developed by Cortese and Balachandar (1995) . The flow of interest is periodic in both streamwise and spanwise directions and hence Fourier expansions are implemented in these two directions. The top and bottom boundaries are specified to be wall boundaries and in this study a 6th-order compact difference scheme is implemented on a Chebyshev grid. We first introduce the governing equation in Fourier space and then

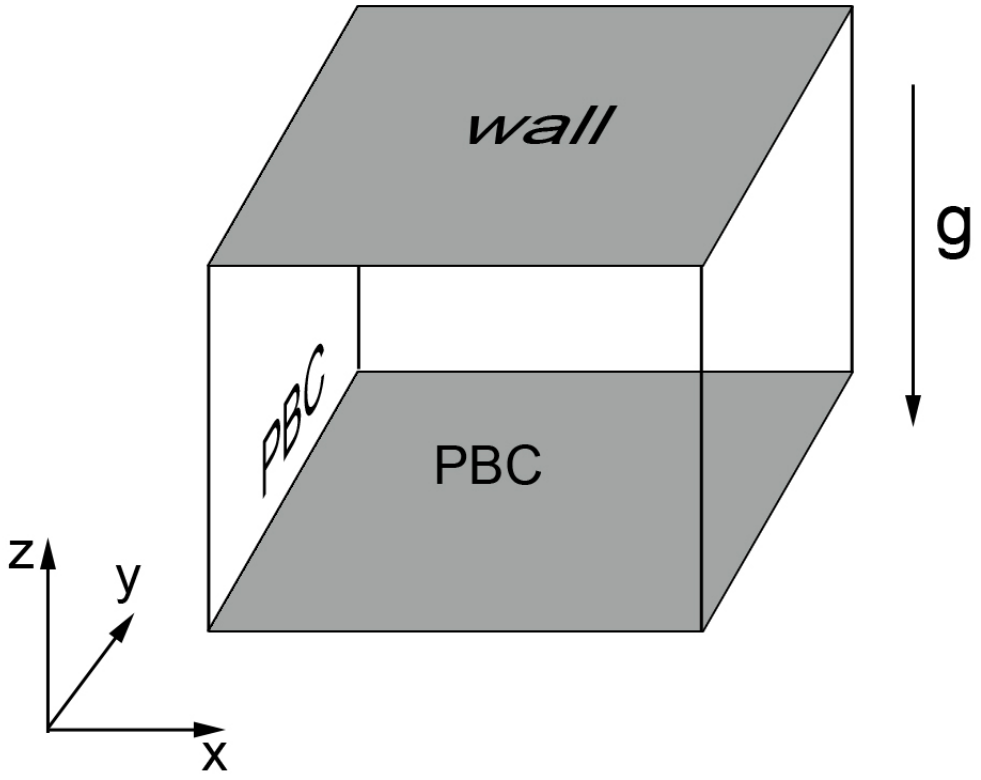

Figure 1: Sketch of the computational domain.

the time integration and the spatial discretization are discussed.

3.1 Fourier expansion

As figure 1 shows, the flow is periodic in both stream-wise and span-wise directions, therefore, Fourier expansion is implemented in these directions to enforce the periodic boundary condition. In the vertical direction, no-slip and no-penetration velocity boundary conditions are implemented for the wall boundary conditions. We employed a 6th order compact finite difference scheme, which will be discussed later. The velocity field

can, therefore, be written as

$$\mathbf{u}(x,y,z;t) = \sum_{k_x}\sum_{k_y} \hat{\mathbf{u}}(k_x,k_y,z;t)e^{i(k_x x+k_y y)} \tag{11}$$

with $\hat{\mathbf{u}}$ represents the Fourier transform of $\mathbf{u}$.

To solve the governing equations 7 and 8 with the effective kinematic viscosity and diffusivity as a function of concentration, convolution operation is required in Fourier space for the viscous term. This makes the equations very difficult solve. We decompose the function $f(\phi)$ in real space as $f(\phi) = \bar{f} + f'$, where

$$\bar{f} =< f(\phi) >, \qquad f' = f(\phi) - \bar{f} \tag{12}$$

with $< \cdot >$ signifying the average operation over the $x-y$ horizontal plane. Now equation 7 can be written as

$$\frac{\partial \mathbf{u}}{\partial t} + \mathbf{u}\cdot\nabla\mathbf{u} = -\nabla p + \frac{\bar{f}}{Re}\nabla^2\mathbf{u} + Ri\phi\mathbf{e_3} + \frac{f'}{Re}\nabla^2\mathbf{u} + \frac{2}{Re}\nabla f\cdot\mathbf{S} \tag{13}$$

where $\mathbf{S} = (\nabla\mathbf{u} + \nabla\mathbf{u}^T)/2$ is the strain rate tensor.

By taking the Fourier transform, the above governing equation can be written as

$$\begin{aligned}\frac{\partial \hat{\mathbf{u}}}{\partial t} + \mathcal{F}(\mathbf{u}\cdot\nabla\mathbf{u}) = &-\mathcal{F}(\nabla p) + \frac{\bar{f}}{Re}\left[-(k_x^2+k_y^2) + \frac{\partial^2}{\partial z^2}\right]\hat{\mathbf{u}} + Ri\hat{\phi}\mathbf{e_3} \\ &+ \mathcal{F}\left(\frac{f'}{Re}\nabla^2\mathbf{u} + \frac{2}{Re}\nabla f\cdot\mathbf{S}\right)\end{aligned} \tag{14}$$

with $\mathcal{F}()$ as the Fourier transform operator.

To solve equation (9) for sediment concentration, we can take the same decomposition with $h(\phi) =< h(\phi) > +(h(\phi) - < h(\phi) >) = \bar{h} + h'$, and the governing equation in

Fourier space can be written as

$$\begin{aligned}\frac{\partial\hat{\phi}}{\partial t}+\mathcal{F}(\mathbf{v}\cdot\nabla\phi)=&\frac{\bar{h}}{ReSc}\left[-(k_x^2+k_y^2)+\frac{\partial^2}{\partial z^2}\right]\hat{\phi}\\&+\mathcal{F}\left\{\frac{1}{ReSc}\nabla\cdot(h'\nabla\phi)+\frac{1}{ReSc}\nabla\bar{h}\cdot\nabla\phi\right\}\end{aligned}\tag{15}$$

The nonlinear terms in equation (14) and (15) are calculated in the real space and dealiased using the two-thirds method[*Boyd*(2001), *Moin and Kim*(1982)].

3.2 Time integration

Equation 14 and 15 are solved with a standard projection method. The velocity is first advanced to the intermediate level $\hat{\mathbf{u}}^*$, which is not divergence-free. Subsequently in the correction step, the pressure is solved by the Poisson equation, then the intermediate velocity $\hat{\mathbf{u}}^*$ is projected to the divergence-free field. In this paper, the nonlinear terms are advanced by a third-order low-storage Runge-Kutta method [*Williamson*(1980)], and the semi-implicit second-order Crank-Nicolson scheme is used for the diffusion terms. The viscous terms are treated semi-implicitly in order to relax the strong stability restriction on the time step. For the advection term, Arakawa scheme [*Arakawa and Lamb*(1980)] is implemented, where for odd time step, the advection form is used and for even time step, the divergence form is used.

To simplify the notation, we define the advection operators and the diffusion operator as

$$A(\hat{\mathbf{u}})=-\mathcal{F}[\mathbf{u}\cdot\nabla\mathbf{u}],\quad D(\hat{\mathbf{u}})=\frac{\bar{f}}{Re}\nabla^2\hat{\mathbf{u}}=\frac{\bar{f}}{Re}\left[-(k_x^2+k_y^2)+\frac{\partial^2}{\partial z^2}\right]\hat{\mathbf{u}}\tag{16}$$

Projection method [*Chorin*(1968)] is used to solve the Navier-Stokes equations. The low-storage third order Runge-Kutta method is adopted for the time integral, and in the

prediction step the intermediate velocity is calculated as

$$\hat{\mathbf{u}}^{(\mathbf{0})} = \hat{\mathbf{u}}(t^{(n)}) \tag{17}$$

$$\hat{\mathbf{H}}^{(m)} = \Delta t\left[A(\hat{\mathbf{u}}^{(\mathbf{m-1})}) + Ri\hat{\phi}\mathbf{e}_3 + \mathcal{F}\left(\frac{f'}{Re}\nabla^2\mathbf{u}^{(m-1)} + \frac{2}{Re}\nabla f \cdot \mathbf{S}_{ij}^{(m-1)}\right)\right] + cnl1(m)\hat{\mathbf{H}}^{(m-1)} \tag{18}$$

$$\hat{\mathbf{u}}^{(\mathbf{m*})} = \hat{\mathbf{u}}^{(m-1)} + cnl2(m)\hat{\mathbf{H}}^{(m)} + cd(m)[D(\hat{\mathbf{u}}^{(m-1)}) + D(\hat{\mathbf{u}}^{(m*)})] \tag{19}$$

At this point, the intermediate velocity is not divergence-free. In the correction step, pressure Poisson equation is first solved, then the velocity field is projected to the divergence-free field. The correction step can be written as:

$$\nabla^2\hat{p} = \frac{1}{2cd(m)}\nabla \cdot \hat{\mathbf{u}}^{(m*)} \tag{20}$$

$$\hat{\mathbf{u}}^{(m)} = \hat{\mathbf{u}}^{(m*)} - 2cd(m)\nabla\hat{p} \tag{21}$$

$$\hat{\mathbf{u}}(t^{(n+1)}) = \hat{\mathbf{u}}^{(3)} \tag{22}$$

where $m = 1, 2, 3$ and $cnl1 = \{0, -5/9, -153/128\}$, $cnl2 = \{1/3, 15/16, 8/15\}$, $cd = \{\Delta t/6, 5\Delta t/24, \Delta t/8\}$ with Δt the time-step. The super script * means variables at the intermediate step. For our study, the time step is chosen based on CFL criterion.

3.3 Spatial discretization

A 6th order centered compact finite difference scheme is implemented in the vertical direction in this study. A general compact finite difference scheme for one-dimensional problems centered at x_i has the form

$$u_i^{(p)} + \sum_{j\in I_n} a_j u_j^{(p)} = \sum_{j\in I_n} b_j u_j + \sum_{j\in I_m} b_j u_j \tag{23}$$

where u_j are the function values given at the grid points $x_j \in I_n \cup I_m$ and $u_j^{(p)}$ are the values of the p-th derivative of the function given at the grid points $x_j \in I_n$. For the boundary layer flow, finer grid is required near the wall, therefore, non-uniform grid is preferred for both computational efficiency and numerical stability. For high order compact finite difference scheme on non-uniform grid, we need to solve for the coefficients a_j and b_j. If Taylor's expansion is used to solve for these coefficients, the problem can be ill-conditioned and the results will be contaminated by the numerical errors[*Shukla and Zhong*(2005)]. A general derivation of the compact finite difference scheme on non-uniform grid based on Lagrangian Polynomial is given by [*Shukla and Zhong*(2005)]. The use of non-uniform grid also can alleviate the numerical instability arising from the boundary treatment of compact finite difference schemes [*Pereira et al.*(2001), *Shukla and Zhong*(2005)]. A tridiagonal 6th order compact finite difference scheme is implemented in this study, where the point sets are chosen as $I_m = \{i-2, i, i+2\}$ and $I_n = \{i-1, i+1\}$. Centered schemes are implemented for the interior region, and one-sided scheme is utilized around the boundary. For the interior grids, we have

$$a_{i-1}u'_{i-1} + u'_i + a_{i+1}u'_{i+1} = b_{i-2}u_{i-2} + b_{i-1}u_{i-1} + b_i u_i + b_{i+1}u_{i+1} + b_{i+2}u_{i+2}$$
$$c_{i-1}u''_{i-1} + u''_i + c_{i+1}u''_{i+1} = d_{i-2}u_{i-2} + d_{i-1}u_{i-1} + d_i u_i + d_{i+1}u_{i+1} + d_{i+2}u_{i+2}$$

with a, b, c and d derived based on Lagrangian Polynomials [*Shukla and Zhong*(2005)]. The detailed derivation following [*Shukla and Zhong*(2005)] can be found in the Appendix. At the bottom wall boundaries, an one-sided scheme is used to keep the 6th

order accuracy:

$$
\begin{aligned}
a_1 u_1' + u_2' + a_3 u_3' &= b_1 u_1 + b_2 u_2 + b_3 u_3 + b_4 u_4 + b_5 u_5 \\
u_1' + a_2 u_2' &= b_1 u_1 + b_2 u_2 + b_3 u_3 + b_4 u_4 + b_5 u_5 + b_6 u_6 \\
c_1 u_1'' + u_2'' + c_3 u_3'' &= d_1 u_1 + d_2 u_2 + d_3 u_3 + d_4 u_4 + d_5 u_5 \\
u_1'' + c_2 u_2'' &= d_1 u_1 + d_2 u_2 + d_3 u_3 + d_4 u_4 + d_5 u_5 + d_6 u_6
\end{aligned}
$$

and at the top boundary, we have

$$
\begin{aligned}
a_{N-2} u_{N-2}' + u_{N-1}' + a_N u_N' &= b_{N-4} u_{N-4} + b_{N-3} u_{N-3} + b_{N-2} u_{N-2} + b_{N-1} u_{N-1} + b_N u_N \\
u_N' + a_{N-1} u_{N-1}' &= b_{N-5} u_{N-5} + b_{N-4} u_{N-4} + b_{N-3} u_{N-3} + b_{N-2} u_{N-2} + b_{N-1} u_{N-1} + b_N u_N \\
c_{N-2} u_{N-2}'' + u_{N-1}'' + c_N u_N'' &= d_{N-4} u_{N-4} + d_{N-3} u_{N-3} + d_{N-2} u_{N-2} + d_{N-1} u_{N-1} + d_N u_N \\
u_N'' + c_{N-1} u_{N-1}'' &= d_{N-5} u_{N-5} + d_{N-4} u_{N-4} + d_{N-3} u_{N-3} + d_{N-2} u_{N-2} + d_{N-1} u_{N-1} + d_N u_N
\end{aligned}
$$

3.4 Matrix formulation

It is useful to rewrite the compact finite difference schemes in matrix form for the solution of the velocity Helmholtz equation and the pressure Poisson equation. The matrix form of the first and the second order derivatives are

$$
\mathbf{A_1} f' = \mathbf{B_1} f, \quad \mathbf{A_2} f'' = \mathbf{B_2} f \tag{24}
$$

with $'$ signifying the derivative with respect to z. The first derivative can be written as

$$
f' = \mathbf{A_1}^{-1} \mathbf{B_1} f \tag{25}
$$

Although matrix $\mathbf{A_1}$ is a tridiagonal matrix, the inverse of $\mathbf{A_1}$ is a dense matrix. Therefore, the product ${\mathbf{A_1}}^{-1}\mathbf{B_1}$ is also a dense matrix. The same applies to the second order derivatives. To take full advantage of banded property of matrix $\mathbf{A_1}$, $\mathbf{A_2}$ and $\mathbf{B_1}$, $\mathbf{B_2}$, the numerical solution of the semi-discrete Helmhotz equation is accomplished by LU decomposition with pivoting.

The semi-implicit time-integration method leads to a Helmholtz equation for the velocity field in the prediction step. The diffusion operator can be written as $D() = \mathbf{D}{\mathbf{A_2}}^{-1}\mathbf{B_2} - (k_x^2 + k_y^2)\mathbf{D}$, where $\mathbf{D} = diag(\bar{f}_i/Re)$, and equation 19 now becomes

$$D(\hat{\mathbf{u}}^{(m*)}) - \frac{\hat{\mathbf{u}}^{(m*)}}{cd(m)} = \hat{\mathbf{b}}$$

where $\hat{\mathbf{b}} = -[\hat{\mathbf{u}}^{(m-1)} + cnl2(m)\hat{\mathbf{H}}^{(m)}]/cd(m) - D(\mathbf{u}^{(m-1)})$. We can then re-write the above system as

$$\mathbf{D}{\mathbf{A_2}}^{-1}\left[\mathbf{B_2} - (k_x^2 + k_y^2)\mathbf{A_2} - \frac{1}{cd(m)}\mathbf{A_2}\mathbf{D}^{-1}\right]\hat{\mathbf{u}}^{(m*)} = \hat{\mathbf{b}} \tag{26}$$

where $\mathbf{A_2}$ and $\mathbf{B_2}$ are both banded matrix. Thus, the final form can be written as

$$\mathbf{C}\hat{\mathbf{u}}^{(m*)} = \hat{\mathbf{b}}' \tag{27}$$

where $\hat{\mathbf{b}}' = \mathbf{A_2}\mathbf{D}^{-1}\hat{\mathbf{b}}$, and $\mathbf{C} = \mathbf{B_2} - (k_x^2 + k_y^2)\mathbf{A}_2 - \mathbf{A}\mathbf{D}^{-1}/cd(m)$. $\mathbf{C}$ is also a banded matrix, the above equation can be direct solved using LU decomposition method (dgbsv from LAPACK package).

In the correction step, projection method is used and pressure Poisson equation need to be solved. The pressure Poisson equation is written as

$$\nabla^2\hat{p} = \frac{1}{2cd(m)}(\hat{u}_x + \hat{v}_y + \mathbf{A_1^{-1}}\mathbf{B_1}\hat{w}) \tag{28}$$

where $\hat{u}_x = -ik_x\hat{u}$ and $\hat{v}_y = -ik_y\hat{v}$ in Fourier space. It has been pointed out that for compact finite difference scheme, the second order derivative discretization is not compatible with the first order derivative discretization [*Boersma*(2011)], which means

$$\mathbf{A_2^{-1}B_2}f \neq \mathbf{A_1^{-1}B_1}(\mathbf{A_1^{-1}B_1}f) \tag{29}$$

This will introduce large numerical error if we direct use the second order derivative scheme to solve the pressure Poisson equation and correct the velocity filed using the first order derivative scheme. The right discretization for the pressure Poisson equation [*Boersma*(2011)] will be

$$-(k_x^2 + k_y^2)\hat{p} + \mathbf{A_1^{-1}B_1}(\mathbf{A_1^{-1}B_1}\hat{p}) = \frac{1}{2cd(m)}(\hat{u}_x + \hat{v}_y + \mathbf{A_1^{-1}B_1}\hat{w}) \tag{30}$$

For medium sized problem (number of grid points in vertical direction N_z not very large), direct solver is affordable and implemented in our study. Define $\mathbf{F} = (\mathbf{A_1^{-1}B_1})^2$, and take the eigen-decomposition (dgeev from LAPACK package), we obtain

$$\mathbf{F} = \mathbf{R\Lambda R}^{-1} \tag{31}$$

where $\mathbf{\Lambda}$ is a diagonal matrix with the eigen values of matrix $\mathbf{F}$ as its elements. The above Eq. (30) now writes

$$\mathbf{R}(\mathbf{\Lambda} - (k_x^2 + k_y^2)\mathbf{I})\mathbf{R}^{-1}\hat{p} = \frac{1}{2cd(m)}(\hat{u}_x + \hat{v}_y + \mathbf{A_1^{-1}B_1}\hat{w}) \tag{32}$$

and can be solved with given $\mathbf{R}$, $\mathbf{\Lambda}$ and $\mathbf{R}^{-1}$.

3.5 Boundary conditions

Flow velocity field $\mathbf{u}$ satisfies no-slip and no-penetration boundary conditions at the wall boundaries. Because the projection method separates the momentum equation into two parts, the no-slip boundary condition and incompressibility condition can not be satisfied simultaneously. A proper choice of boundary conditions for the intermediate velocity $\tilde{\mathbf{u}}$ must be made in order to minimize the slip at the correction step. A boundary condition for pressure must also be specified. It can be shown that although there is no natural boundary condition for pressure, a self-consistent, pure Neumann condition will allow the slip velocity to be minimized.

An analysis of the pressure part of the time splitting routine yields all the necessary boundary conditions. Defining τ to be the unit vector tangential to the wall, the tangential component of the pressure correction step is

$$\tau \cdot \mathbf{u}^{(\mathbf{m})}|_{z=\pm 1} = \tau \cdot [\mathbf{u}^{(m*)} - 2cd(m)\nabla p^{(m)}]|_{z=\pm 1} \tag{33}$$

The no-slip condition requires the left hand side of equation 33 to be zero. This can be used to obtain the boundary condition of the intermediate velocity $\tilde{\mathbf{u}}$ as

$$\tau \cdot \mathbf{u}^{(m*)}|_{z=\pm 1} = 2cd(m)\tau \cdot \nabla p^{(m)}|_{z=\pm 1} \tag{34}$$

Because the pressure $p^{(m)}$ has not yet been computed when the intermediate velocity $\mathbf{u}^{(m*)}$ is calculated with the corresponding boundary condition needed, an approximation of $\nabla p^{(m)}$ must be used instead. A second order accurate approximation is used in this study, which gives

$$\nabla p^{(m)} = \nabla p^{(m-1)}\left[1 + \frac{cd(m)}{cd(m-1)}\right] - \nabla p^{(m-2)}\left[\frac{cd(m)}{cd(m-1)}\right] + O(\Delta t^2) \tag{35}$$

Hence, the corresponding boundary conditions for the intermediate velocity component are

$$u^{(m*)}|_{z=\pm1} = 2cd(m)\left\{\frac{\partial p^{(m-1)}}{\partial x}\left[1+\frac{cd(m)}{cd(m-1)}\right]-\frac{\partial p^{(m-2)}}{\partial x}\left[\frac{cd(m)}{cd(m-1)}\right]\right\}\Bigg|_{z=\pm1} \tag{36}$$

$$v^{(m*)}|_{z=\pm1} = 2cd(m)\left\{\frac{\partial p^{(m-1)}}{\partial y}\left[1+\frac{cd(m)}{cd(m-1)}\right]-\frac{\partial p^{(m-2)}}{\partial y}\left[\frac{cd(m)}{cd(m-1)}\right]\right\}\Bigg|_{z=\pm1} \tag{37}$$

Moreover, the pure Neumann boundary condition for the pressure field

$$\left.\frac{\partial p^{(m)}}{\partial z}\right|_{z=\pm1} = 0 \tag{38}$$

gives the boundary condition for the vertical component of intermediate velocity

$$w^{(m*)}|_{z=\pm1} = 0 \tag{39}$$

For sediment concentration, the boundary condition at both the top and bottom boundaries are given as

$$-W_s\phi + \frac{1}{ReSc}\frac{\partial\phi}{\partial z} = 0 \tag{40}$$

with the diffusivity of sediment set to be a constant in this study. This boundary condition imposes no net deposition and suspension from the well boundary. It allows the total mass of sediment in the computational domain to be conserved throughout the computation.

3.6 Numerical analysis in the wall normal direction

In this section, we demonstrate the numerical accuracy of the present sixth-order compact finite difference scheme on Chebyshev grid points. When a high order boundary closure is implemented on a uniform grid in compact finite difference scheme, oscillations arise at the boundaries. There have been plenty of studies focused on the nu-

merical instability associated with the high-order boundary closures[*Colonius*(2004), *Zhong and Tatineni*(2003), *Shukla and Zhong*(2005)]. By utilizing a non-uniform grid which high resolution clusters at the boundaries, it has been shown that stable high-order boundary closures with the same order of accuracy as the interior points can be achieved [*Zhong and Tatineni*(2003), *Shukla and Zhong*(2005)]. The stable high order compact schemes on non-uniform grids can be derived based on the Lagragian interpolation polynomials [*Shukla and Zhong*(2005)].

To resolve the near-wall turbulence in a boundary layer, fine resolution is required very near the wall. It is common to adopt the non-uniform Chebyshev grid, where grid points cluster at the boundaries. In this study, the Chebyshev grid is implemented in the direction normal to the wall, which is given as

$$z_i = \cos(\pi i/N), \quad i = 0, ..., N \tag{41}$$

with $N_z = N+1$ represents the total number of grid points in the z-direction. Compared to compact schemes, standard finite difference schemes require more neighboring points in order to achieve the same order of accuracy. For the same stencil size discussed in Section 3.3, the standard finite difference scheme is only of 4th order accuracy. Here, Fourier analysis on the Chebyshev grid is applied to study the dispersive and dissipative errors of the compact finite difference schemes implemented in this study. Comparison between the standard finite difference schemes and the compact schemes are made to demonstrate the advantage of adopting a compact finite difference scheme. For the trial function $u(x) = e^{ikx}$, the exact solutions of the first and the second derivatives of $u(x)$ are $iku(x)$ and $-k^2u(x)$. The first order derivative computed by the compact finite difference scheme at nodes x_i is in the form of $ik'e^{ikx_i}$ with k' the modified wave

number

$$k' = -i\frac{b_{i-2}e^{ik(x_{i-2}-x_i)} + b_{i-1}e^{ik(x_{i-1}-x_i)} + b_i + b_{i+1}e^{ik(x_{i+1}-x_i)} + b_{i+2}e^{ik(x_{i+2}-x_i)}}{1 + a_{i-1}e^{ik(x_{i-1}-x_i)} + a_{i+1}e^{ik(x_{i+1}-x_i)}} \tag{42}$$

The dispersive and dissipative errors are given by the real part of $k' - k$, i.e., $\mathbf{Re}(k' - k)$, and the imaginary part $\mathbf{Im}(k' - k)$, respectively. In the present nonuniform grid, the dispersive and dissipative errors also depend on the location of the grid points. The maximum dispersion error and dissipation error for the first-order derivative are presented in figure 2 with $N_z = 65$, where h is the largest grid spacing for the Chebyshev grids. Results of compact finite difference scheme are compared with those of standard finite difference scheme with the same stencil size, which is 4th order accurate. It is clear that the compact finite difference scheme performs much better in terms of both dispersive and dissipative errors, especially at high wavenumber. The compact finite difference scheme almost follows the exact solution to around $kh \approx 2$ while results of the 4th order standard finite difference scheme deviate from the exact solution at $kh \approx 1$. Hence, further grid refinement is required (i.e., more computational efforts) for standard finite difference scheme in order to achieve the same accuracy of compact scheme.

The second-order derivative calculated by the compact finite difference scheme is in the form of $-k''e^{ikx_i}$

$$k'' = -\frac{d_{i-2}e^{ik(x_{i-2}-x_i)} + d_{i-1}e^{ik(x_{i-1}-x_i)} + d_i + d_{i+1}e^{ik(x_{i+1}-x_i)} + d_{i+2}e^{ik(x_{i+2}-x_i)}}{1 + c_{i-1}e^{ik(x_{i-1}-x_i)} + c_{i+1}e^{ik(x_{i+1}-x_i)}}. \tag{43}$$

Figure 3 shows the dispersive and dissipative error for the second order derivative. Similar conclusion can be drawn that the compact finite difference scheme outperforms the standard finite difference scheme for the same stencil size.

We also carry out a convergence test for the Chebyshev grid and compact finite difference scheme used in this study (see Figure 4). The test function is chosen as $f(z) = \sin(\pi z)$. The number of grid points are chosen from 17 to 129. For the first

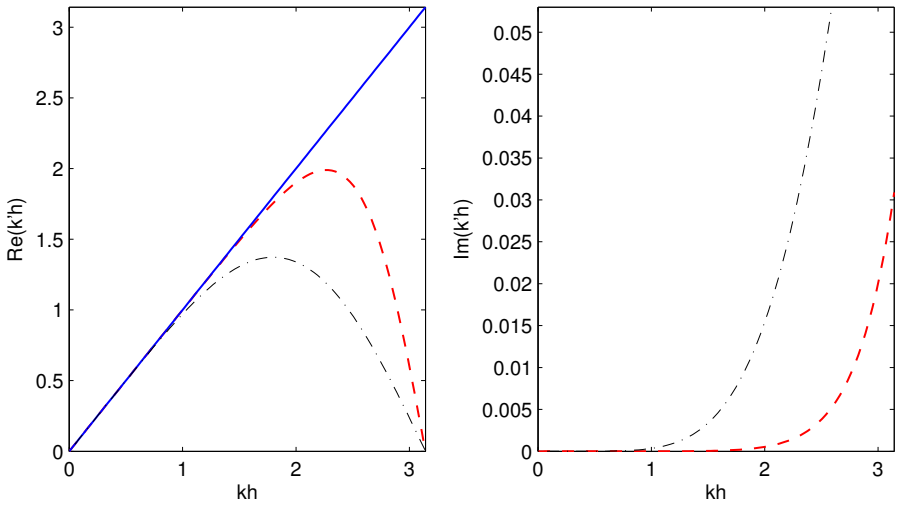

Figure 2: Modified wavenumber for the first order derivative.

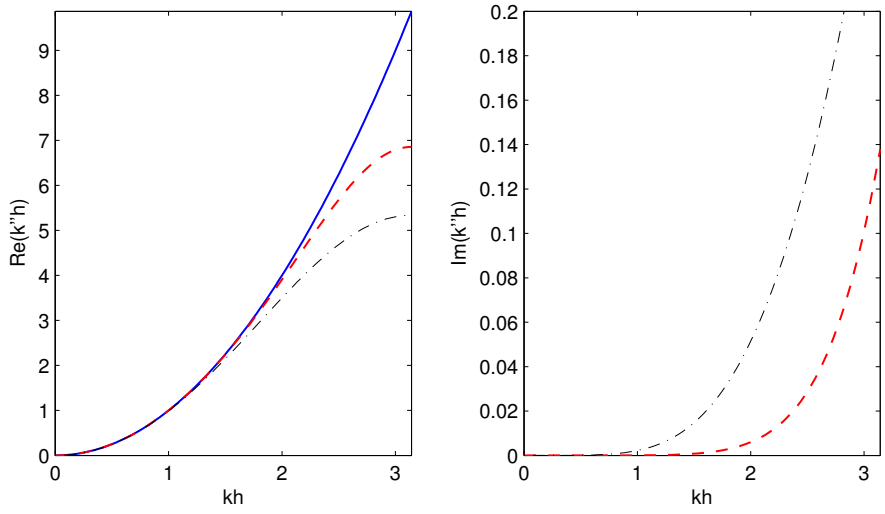

Figure 3: Modified wavenumber for the second order derivative.

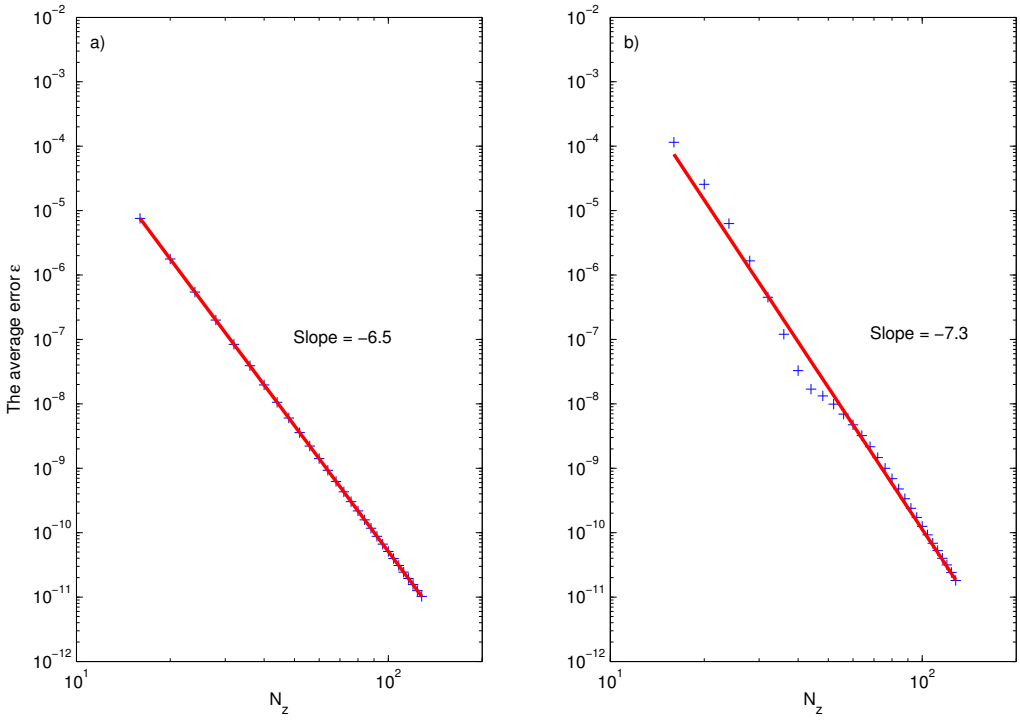

Figure 4: Convergence test of the first order derivative (a) and the second order derivative (b). The test function is chosen as $f(z) = sin(\pi z)$, with the derivatives as $f'(z) = \pi cos(\pi z)$ and $f''(z) = -\pi^2 sin(\pi z)$. The average error is defined by equation 49.

derivative (see Figure 4(a)), the results give a slope of -6.5, while for the second derivative the results give a slope of -7.3 (see Figure4(b)). Analyses present here are consistent with the order of accuracy of the sixth-order compact finite difference scheme implemented in this study.

4 Results

Detailed validations of the present numerical model is presented in Section 4.1. The numerical model is then used to investigate the effect of rheological stress and turbulence modulation in determining the transition of the turbulent and laminar states due to the

presence of sediments the bottom boundary layer (Section 4.2).

4.1 Model Verification

Two verifications/validations of the numerical model developed in this study are presented in this section. The numerical model is first verified with a laminar boundary layer with simple sediment distribution and rheology closure where analytical solutions are available (Section 5.1.1). In Section 5.1.2, we carry out Direct Numerical Simulation of clear fluid channel flow with Reynolds number $Re = \tilde{u}_* H/\nu = 180$ calculated based on friction velocity $\tilde{u}_*$ and channel half-depth H. The present model results are verified with earlier DNS results based on a pseudo-spectral method ([*Kim et al.*(1987)]).

4.1.1 Analytic solution of Poiseuille flow with simple rheology

We consider a pressure driven Poiseuille flow loaded with neutrally buoyant sediment particles. The flow is laminar and homogeneous in both streamwise and spanwise directions. By specifying the boundary condition for sediment concentration as $\tilde{\phi}|_{\tilde{z}=-1} = 0, \tilde{\phi}|_{\tilde{z}=1} = \Phi_0$ and assume a constant diffusivity with $Sc = 0.5$, the solution for sediment concentration profile is written as

$$\tilde{\phi} = \Phi_0(\tilde{z}+1)/2 \tag{44}$$

Utilizing the effective viscosity provided by Einstein's formula $\nu(\tilde{\phi}) = \nu_0(1 + 5/2\tilde{\phi})$ [*Einstein*(1906)]. The governing equation for Poesuille flow now writes

$$\frac{\partial}{\partial\tilde{z}}\left(\nu\frac{\partial\tilde{u}}{\partial\tilde{z}}\right) = \frac{1}{\rho_0}\frac{d\tilde{P}}{d\tilde{x}} \tag{45}$$

where $dP/d\tilde{x}$ is a constant.

The boundary conditions for velocity are no-slip at both top and bottom wall, i.e. $\tilde{u}|_{\tilde{z}=\pm1} =$

0. Defining $\beta = \dfrac{1}{\rho_0 \nu}\dfrac{d\tilde{P}}{d\tilde{x}}$, the analytic solution for the velocity profile is

$$\tilde{u} = \frac{-\beta(\tilde{z}-1)\ln(4) - \beta(\tilde{z}+1)\ln(4+10\Phi_0) + 2\beta\ln(4+5\Phi_0(\tilde{z}+1))}{5\Phi_0(\ln(4)-\ln(4+10\Phi_0))} \tag{46}$$

We also include another commonly used rheology closure of Krieger-Dougherty (1959) based on a power law

$$\nu = \nu_s\left(1-\frac{\tilde{\phi}}{\phi_m}\right)^{-[\eta]\phi_m} \tag{47}$$

For cohesionless spherical particles, we use $[\eta]\phi_m = 2.0$ and $\phi_m = 0.61$. In this case, the analytic solution for the velocity profile can also be given as

$$\tilde{u} = \frac{a_0 + a_1\tilde{z} + a_2\tilde{z}^2 + a_3\tilde{z}^3 + a_4\tilde{z}^4}{16(3-3\alpha+\alpha^2)} \tag{48}$$

with $\alpha = \Phi_0/\phi_m$ and

$$\begin{aligned}
a_0 &= -24\beta + 48\alpha\beta - 33\alpha^2\beta - 9\alpha^3\beta + \alpha^4\beta \\
a_1 &= 24\alpha^2\beta - 16\alpha\beta - 12\alpha^3\beta + 2\alpha^4\beta \\
a_2 &= 24\beta - 48\alpha\beta + 30\alpha^2\beta - 6\alpha^3\beta \\
a_3 &= 16\alpha\beta - 24\alpha^2\beta + 12\alpha^3\beta - 2\alpha^4\beta \\
a_4 &= 3\alpha^2\beta - 3\alpha^3\beta + \alpha^4\beta
\end{aligned}$$

We solve the problem using the sixth-order tridiagonal compact schemes with $N_x = 32$ and $N_y = 32$. In the vertical direction, the non-uniform grid is applied with $N_z =$ 33, 49, 65, 97 and 129. To quantify the accuracy, the average error is defined as

$$\epsilon = \frac{\sqrt{\sum_{i=0}^{N_z}(<\tilde{u}>_i - \tilde{u}_{exact})}}{N_z} \tag{49}$$

Figure 5 shows the comparison of model results with analytical solution with $\Phi_0 = 1\%$

N_z	$\epsilon_E(\Phi_0 = 1\%)$	$\epsilon_E(\Phi_0 = 5\%)$	$\epsilon_{KD}(\Phi_0 = 1\%)$	$\epsilon_{KD}(\Phi_0 = 5\%)$
33	2.50×10^{-12}	1.34×10^{-12}	1.61×10^{-10}	1.01×10^{-12}
49	2.43×10^{-12}	8.50×10^{-13}	1.33×10^{-10}	7.27×10^{-13}
65	1.67×10^{-12}	5.56×10^{-13}	1.16×10^{-10}	5.30×10^{-13}
97	1.81×10^{-12}	7.83×10^{-13}	9.48×10^{-11}	8.87×10^{-13}
129	1.31×10^{-12}	8.42×10^{-13}	3.55×10^{-9}	9.38×10^{-13}

Table 1: Results obtained from the numerical solution using Einstein's and Krieger-Dougherty rheology model. Here n denotes the number of grid points in vertical direction. ϵ is the error defined by above equation with $\Phi_0 = 1\%$ and $\Phi_0 = 5\%$. The subscript $_E$ and $_{KD}$ denote the Einstein and Krieger-Dougherty rheology model, respectively.

and $\Phi_0 = 5\%$. By introducing the rheological stress, the mean velocity profile starts to show asymmetry, especially for $\Phi_0 = 5\%$. Table 4.1.1 shows the results of grid refinement test. The model results show excellent agreement with the analytical solutions even when the number of grid points N_z is as low as 33. At low concentration, the numerical model performs better with Einstein's rheology model because the Einstein's rheology model is a linear function of sediment concentration ϕ while the Krieger-Dougherty rheology model is a nonlinear function of sediment concentration ϕ. For both rheology models, the numerical model produces smaller numerical errors with higher sediment concentration Φ_0.

4.1.2 Direct numerical simulations of channel flow at *Re*=180

There has been many laboratory experiment ([*Comte-Bellot*(1963), *Eckelmann*(1974), *Wei and Willmarth*(1989)]) and numerical ([*Kim et al.*(1987), *Moser and Moin*(1987), *Moin and Kim*(1982)]) studies of fully developed turbulent channel flow. The second model verification/validation reported here is the steady fully developed channel flow at Reynolds number $Re = 180$. The Reynolds number is defined as

$$Re = \frac{\tilde{u}_* H}{\nu} \tag{50}$$

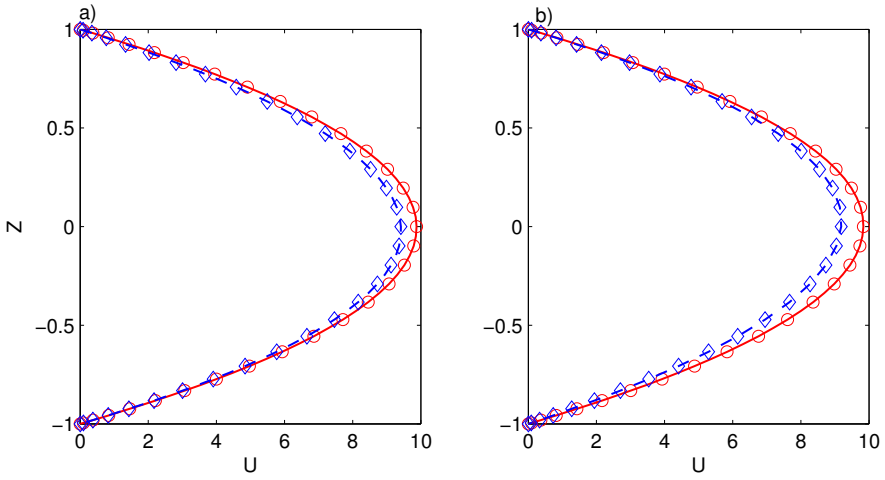

Figure 5: Model results compared with analytical solution. a) Einstein's rheology model. b) Kreiger-Dougherty rheology model. Solid lines are analytical solution with $\Phi_0 = 1\%$, dash lines are analytical solution with $\Phi_0 = 5\%$, circles represent model results with $\Phi_0 = 1\%$ and diamonds represent model results with $\Phi_0 = 5\%$.

where H is the half depth of the channel, and $\tilde{u}_*$ is the friction velocity (the Reynolds number become 3240 if using the center-line velocity). At $Re = 180$, data obtained from direct numerical simulation with a pseudo-spectral scheme is available ([*Kim et al.*(1987)]). The fully developed channel flow is homogeneous in both streamwise and the spanwise directions. The computational domain is chosen as $4\pi H$ and $2\pi H$ in the streamwise and the spanwise direction, respectively, to assure the domain size is greater than the largest eddies in the flow. Figure 6 shows a sketch of the computational domain and the coordinate system. The computation domain is discretized using $N_x \times N_y \times N_z = 128 \times 128 \times 193$ grid points. Channel flow studies typically use wall unit to present the result, with $z^+ = \tilde{z}\tilde{u}_*/\nu$ [*Kim et al.*(1987), *Moin and Kim*(1982)]. In this study, the first grid point away from the wall is at $z^+ \approx 0.02$, and the maximum spacing is about 2.9 wall units near the centerline of the channel. The grid resolution can be shown to be sufficiently fine to resolve all the essential turbulent scales and no sub-grid closure is needed [*Moin and Kim*(1982)].

In this study, the statistically-averaged mean flow quantities are computed by averaging

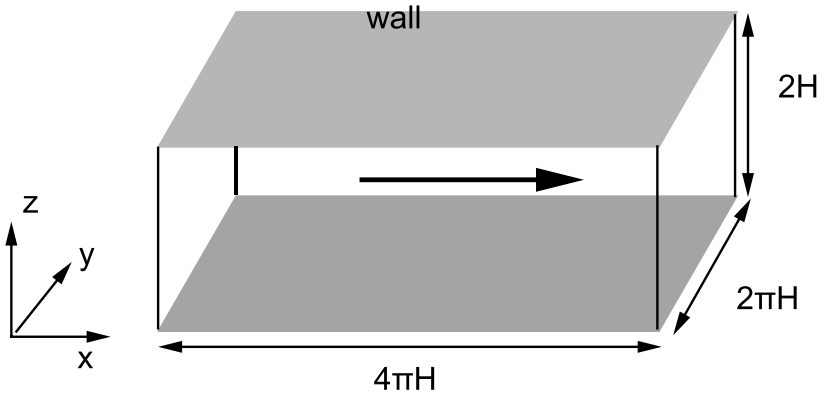

Figure 6: A sketch of the model domain for channel flow. Periodic boundary conditions are implemented for the four sides of the box and no-slip wall boundary conditions are implemented for the top and bottom boundaries.

over x-y plane. The average operator $< \cdot >$ is defined as

$$< u >= \frac{1}{L_x L_y} \int \int \int u(x, y, z; t) dx dy \tag{51}$$

Figure 7 present the results of mean velocity. The solid curve shows the numerical results of the present model, the dash curve shows the numerical results by Kim et al. [*Kim et al.*(1987)], and the symbols represent experiment data from Eckelmann [*Eckelmann*(1974)]. Within the viscous sublayer $z^+ < 5$, the present numerical model is able to predict the linear profile well. In the logarithmic region, our model results agree very well with theoretical prediction. Model results also agree with earlier DNS results of [*Kim et al.*(1987)] and laboratory data of [*Eckelmann*(1974)]. Figure 8 shows the nondimensional RMS velocity fluctuations. The present model results agree very well with the numerical solutions of Kim et al. [*Kim et al.*(1987)] based on the more accurate pseudo-spectral scheme. Comparing to measured data [*Eckelmann*(1974)], both models appear to slightly under-predict the RMS velocity fluctuations in spanwise and vertical direction near the wall.

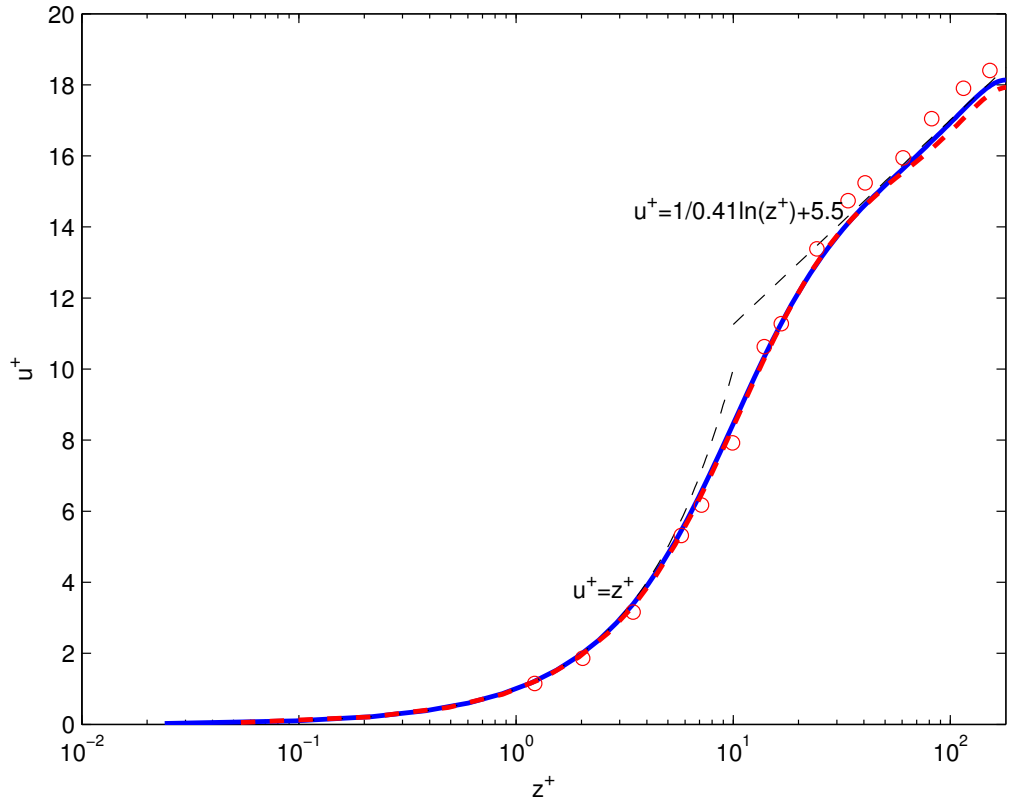

Figure 7: Mean-velocity profiles. Solid line represents model results by the present model, dash line represents model results by Kim et al. [*Kim et al.*(1987)], symbols represent measured data from Eckelmann(1974).

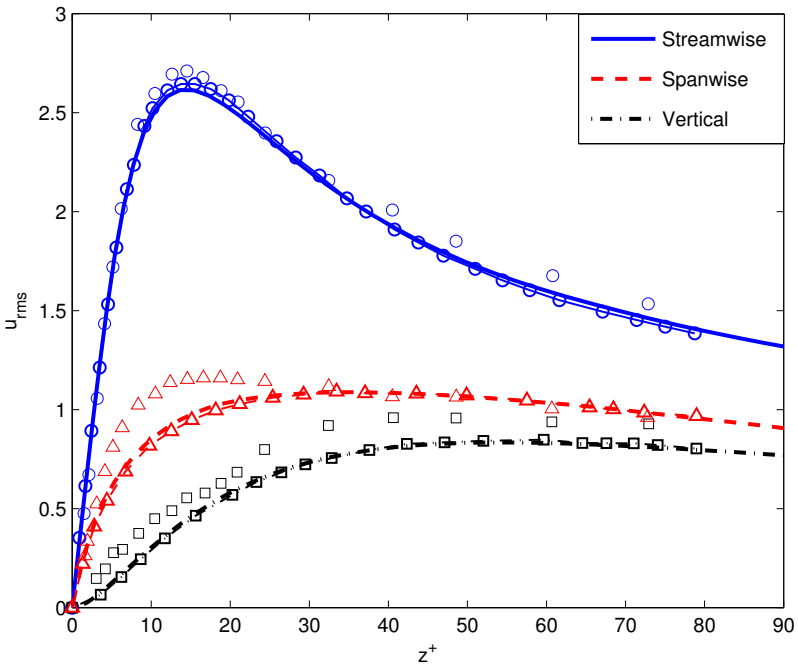

Figure 8: Root-mean-square velocity fluctuations normalized by the wall friction velocity. Symbols represent the data from Kreplin & Eckelmann (1979), lines with symbols represent simulation results by Kim et al. [*Kim et al.*(1987)] using a pseudo-spectral scheme, lines represent simulation results by the present model.

4.2 The effect of rheology

There have been many studies on sediment transport in channel flow [*Hopfinger*(1987), *Zhou and Ni*(1995), *Winterwerp*(2001)] as well as turbidity currents [*Cantero et al.*(2009), *Cantero et al.*(2012)] focusing on the stratification effects on turbulence induced by the suspended fine sediment. For stratified flow, a critical Richardson number can be defined and the turbulent flow field collapses when the Richardson number exceeds this critical value. For sediment-laden steady channel flow or gravity-driven flow, it is proposed that a saturation concentration exists for fine sediment [*Teisson et al.*(1992), *Winterwerp*(2001), *Cantero et al.*(2012)], above which the flow turbulence collapses and the flow start to laminarize. Motivated by these prior studies, we first carry out several numerical experiments for sediment-laden steady channel flow at $Re = 180$ and nondimensional settling velocity of $W_s = 0.02$ without considering the rheological stress. Our simulation results suggest that without including the effect of rheology, the critical Richardson number associated with the saturation concentration for $Re = 180$ and $W_s = 0.02$ (see equation (11)) is around 15. We further investigate the effect of rheology with simulations carried out at $Ri = 11.43$ and volume averaged sediment concentration $\Phi = 1\%$. In summary, four cases are presented here and they are summarized in Table 2. Case 0 is a clear fluid (sediment-free) case at $Re = 180$. Case 1 includes fine sediment with $W_s = 0.02$ but without the effect of rheology. In this case, attenuation of flow turbulence due to sediment-induced density stratification already starts to play a role but the flow remains to be sufficiently turbulent. In Cases 2 and 3, simple rheology model by Krieger and Dougherty [*Krieger and Dougherty*(1959)] is implemented. For cohesive sediments, flocculation produces large and more porous floc aggregates and the value of ϕ_m corresponds to the gelling concentration in which flocs form a space-filling network (e.g., Winterwerp [*Winterwerp*(2002)]). Although flocculation dynamics is not explicitly simulated in this study, we can change ϕ_m value to represent different degree of rheological stress due to flocculation. In this study, we fixed the power $[\eta]\phi_m = 2.0$

and used two different ϕ_m values to investigate the effect of increased effective viscosity. Based on the *Re*, *Ri*, Φ and $W_s = 0.02$ used here, Case 2 with $\phi_m = 0.244$ corresponds to more densely packed floc with averaged floc size of 35 μm. Assuming an averaged primary particle diameter to be 4 μm the resulting fractal dimension n_f is around 2.3, which is representative of typical floc consist of inorganic sediments. On the other hand, Case 3 with $\phi_m = 0.122$ corresponds to more porous, loosely packed flocs with averaged floc size of 50 μm and fractal dimension of 2.0, typical of flocs with higher organic content (e.g., Engel and Schartau [*Engel and Schartau*(1999)]). With lower ϕ_m in Case 3, it is clear that the ehnanced viscosity due to rheology is more intense than that of Case 2.

4.2.1 Mean profiles and turbulent intensities

At Richardson nunmber of *Ri* $= 11.43$, the suppression of turbulence due to sediment-induced density stratification by sediments can be identified from the mean flow statistics (see figure 9(a)). In the lower-half of the channel, the mean velocity starts to lose its symmetry solely due to sediment-induced stratification (see solid curve) and combined stratification and rheology effects (see the dash curve and the dash-dotted curve). In the upper half of the channel, the mean velocity only differs slightly due to lower sediment concentration. Specifically, for the Case 3 with $\phi_m = 0.122$, the velocity in the lower half of the channel derivates considerably from others, suggesting significant effect due to rheological stress. For each case, we can also examine the friction velocity, which is defined as

$$u_* = \sqrt{< f(\phi) > \frac{1}{Re} \frac{d < u >}{dz}} \tag{52}$$

and vertically-averaged flow velocity. Table 4.2.1 shows the computed friction velocity at the bottom wall ($u_{*,b}$) and the top wall ($u_{*,t}$) along with vertically-averaged velocity. The friction velocity at the top wall changes in respond to variation in sediment concentration in the domain. Hence, we can qualitatively understand the process by focusing

the discussion on the friction velocity at the bottom wall. When sediment is added to the system, the friction velocity at the bottom wall drops for about 1% for Case 1 due to sediment-indued stable density stratification suppressing the turbulence. The vertically-averaged mean velocity also increases by about 2% comparing to that of the clear fluid (Case 0), which illustrates the well-known drag reduction. Slight attenuation of turbulence can be seen from the RMS velocity fluctuation profiles presented in Figure (10), especially in the spanwise and vertical directions.

When moderate rheological effect ($\phi_m = 0.244$) is considered in Case 2, which gives enhanced viscosity by about $6 \sim 14\%$ throughout the channel (see figure 9 (c)), the friction velocity is reduced by 3% (see Table 2), suggesting that enhanced viscosity due to Newtonian rheology can further attenuate flow turbulence. However, according the the RMS velocity fluctuation profiles, the reduced turbulence is generally within 10% near the bed (see the dash curves in Figure 10). The computed sediment concentration profile is very close to that without rheology (see Figure 9(b)). Finally, the vertically-averaged flow velocity decreases slighly due to the enhanced mean flow dissipation.

Most notably, for Case 3 with more intense rheological effects ($\phi_m = 0.122$), the enhanced viscosity due to rheology ranges from 40% near the bed and reduces to about 10% near the top wall. Here, we observe a 20% drop of bottom friction velocity (Table 2). In the RMS velocity fluctuation profiles (see the dash-dotted curve in Figure 10), turbulent fluctuations are significantly damped in the lower half of the channel where sediment concentration is more significant. Clearly, significant attenuation of flow turbulence due to enhanced viscosity via rheological stress is observed here. The computed sediment concentration profile shows that large amount of sediment is accumulated near the bottom wall and hence a sharp concentration profile with negative gradient is observed. The shape of sediment concentration profile starts to resemble to that of laminar solution (see symbols in Figure 9(b)), suggesting the onset of laminarization. When the flow turbulence gets attenuated more significantly, the vertical turbulent suspension mechanism is also reduced. This in turn results in an increased effective viscosity, which

further damps flow turbulent. The combined effect of reduced turbulent dissipation and increased mean flow dissipation gives a net increase of vertically-averaged flow velocity of 3 $\%$.

To better illustrate the onset of laminarization in Case 3, Figure 11 shows the mean velocity profile in the lower half of the channel in terms of wall units in a semi-logarithmic plot. The bottom friction velocity associated with each case is used to normalize its velocity profile. Between the velocity profiles of Case 1 and Case 2, very near the wall, a slightly decrease of mean velocity can be identified when enhanced viscosity via the rheology closure is introduced into the simulation. In both cases, we can still identify the existence of the log-layer. The slope (3.47 for Case 1 and 3.77 for Case 2) is larger than that of the clear fluid case, which is 2.5. This is the well-established drag-reduction phenomena where the presence of sediment damps the flow turbulence and the overall effect can be parameterized with a reduced Karman constant. Results from Case 1 suggest damping of turbulence due to sediment induced density stratification reduces Karman constant κ from 0.4 to 0. 288. Mild enhancement of viscosity in Case 2 further reduces κ to 0.265. More importantly, when the effect of Newtonian rheology is further enhanced by using $\phi_m = 0.122$, the log-layer completely disappears in Case 3 (see the dash-dotted curve in Figure 11), suggesting that the flow is undergone considerable turbulence suppression. The disappearance of log-layer, which is consistent with the RMS velocity fluctuation profiles presented in Figure 10), provide further evidence on the onset of laminarization.

4.2.2 Discussion

For boundary layer flow, it has been widely accepted that the auto-generation mechanism of hairpin and quasi-streamwise vortices is vital to sustain the flow turbulence

Case No.	ϕ_m	$u_{*,b}$	$u_{*,t}$	$U = \int_z u dz/2H$
0	-	1.00	1.00	15.95
1	-	0.99	1.04	16.27
2	0.244	0.97	1.00	16.17
3	0.122	0.80	1.09	16.40

Table 2: The friction velocity at both bottom and top for each cases.

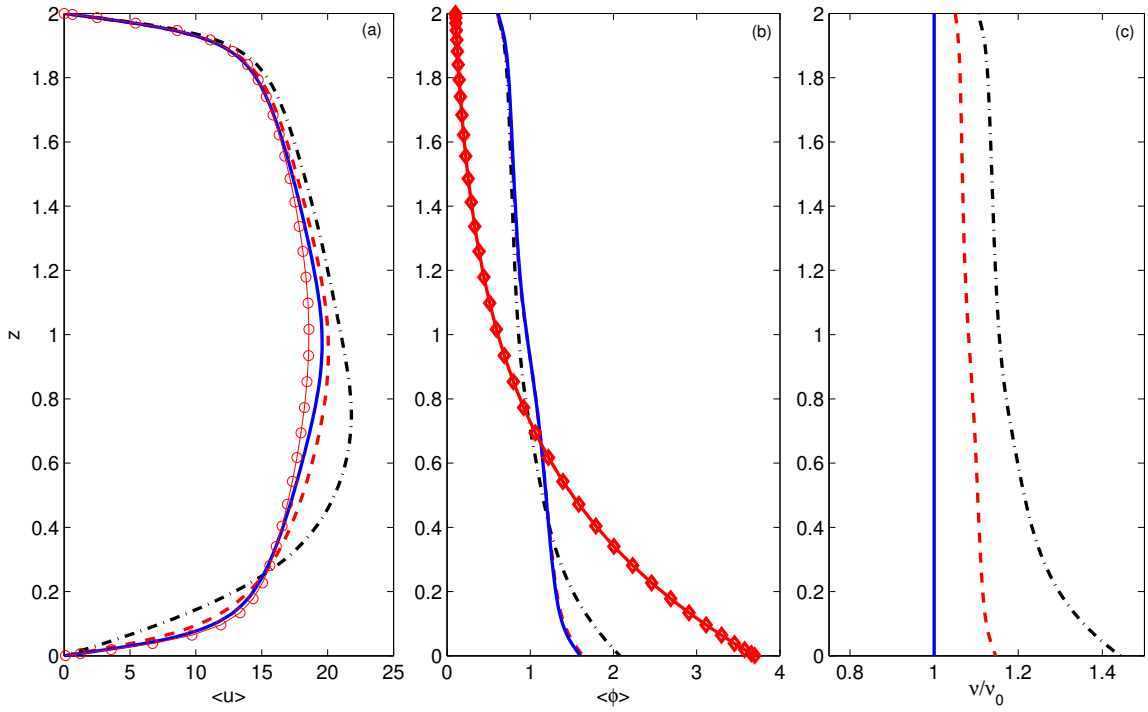

Figure 9: (a) Mean velocity profiles, symbols represent model results of clear fluid, solid line represents model results for simulation without rheology model, dash line represents results from simulation with $\phi_m = 0.244$ and dash-solid line with $\phi_m = 0.122$. (b) Mean sediment concentration profiles, symbols represent laminar solution. (c) Mean effective viscosity profiles, solid line represents model results for simulation without rheology model, dash line represents results from simulation with $\phi_m = 0.244$ and dash-solid line with $\phi_m = 0.122$

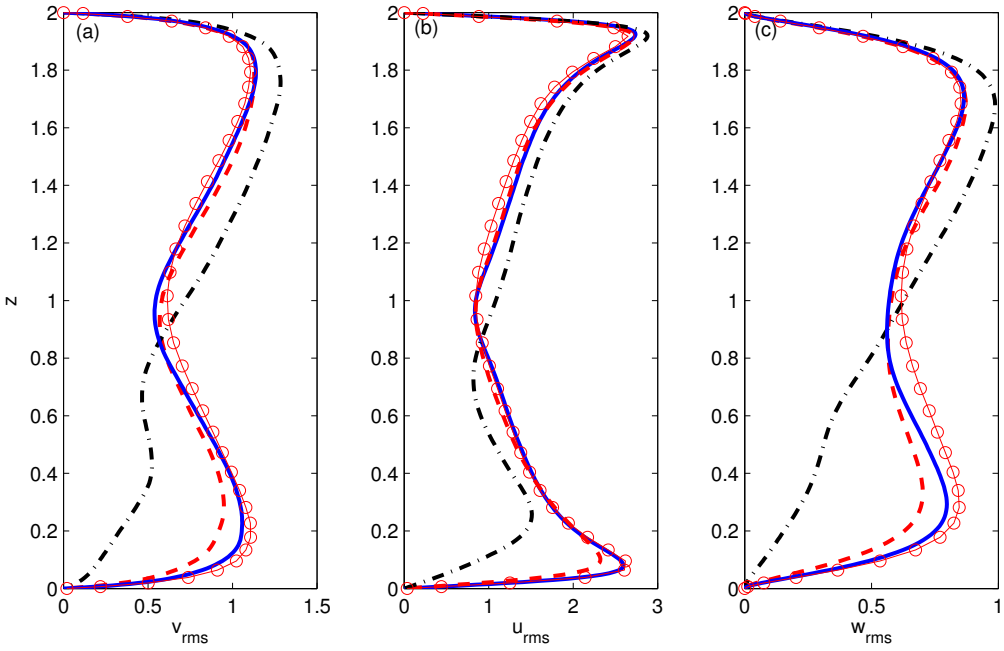

Figure 10: Root mean square velocity profiles, solid line represents model results for simulation without rheology model, dash line represents results from simulation with $\phi_m = 0.244$ and dash-solid line with $\phi_m = 0.122$.

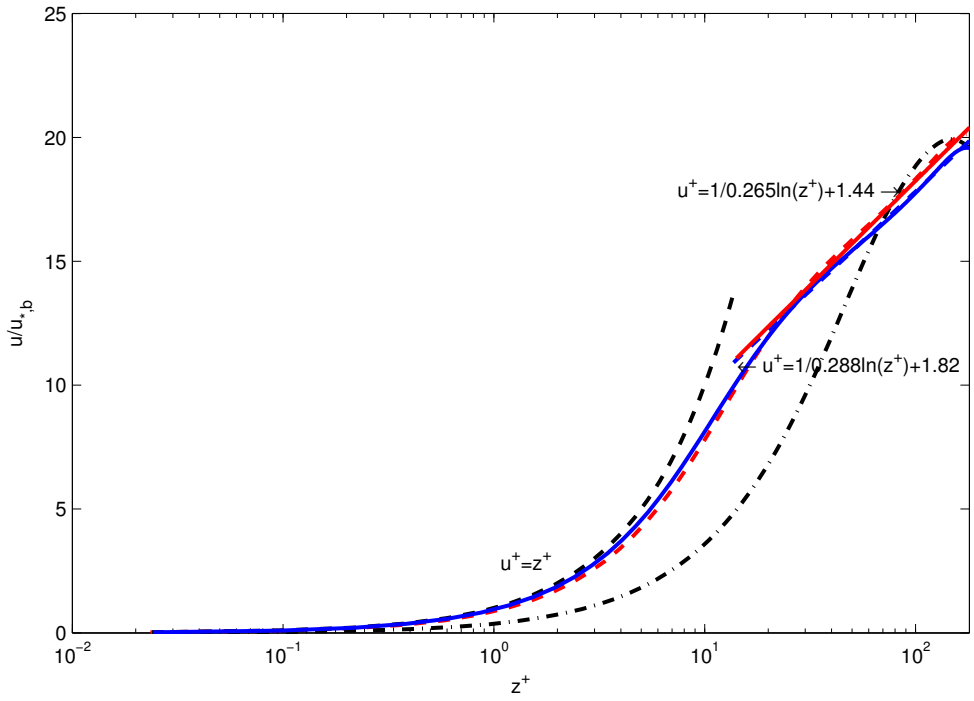

Figure 11: Mean velocity profiles in wall units for different cases, solid line represents model results for simulation without rheology model, dash line represents results from simulation with $\phi_m = 0.244$ and dash-solid line with $\phi_m = 0.122$.

([*Zhou and Ni*(1995), *Zhou et al.*(1999)]). After sediment is added, the generation of hairpin vortices also has to overcome the stabilization effect due to sediment-induced stratification. When sediment concentration is sufficiently large, the vortices are not able to overcome sediment-induced stratification, which leads to collapse of flow turbulence and laminarization. Figure 12 (a) to (c) shows the turbulent coherent structures for Case 1, Case 2 and Case 3, respectively. λ_{ci} method ([*Zhou et al.*(1999)]) is used to identify the vortical structures and only the results in the bottom half of the channel are presented. For Case 1 and Case 2, we observe the vortical structures are more or less populated throughout the whole domain with only slightly less vortical structures in Case 2. However, the vortical structures become much less populated in Case 3 (see Figure 12(c)). When the strength of the vortical structures decreases significantly, the auto-regeneration mechanism breaks down, and the flow tends to laminarize.

The transition from turbulent to laminar state has been attributed to the effect of rheology [*Kessel and Kranenburg*(1996), *Liu and Mei*(1990)] in the context of Bingham plastic rheology and yield stress. In this study, we demonstrate numerically that simply Newtonian rheology with a sufficiently enhanced viscosity can trigger collapse of turbulence and onset of laminarization. Here, it is critical to identify the specific mechanism such that rheological effect with an enhanced viscosity can suppress turbulence. Figure 13 (a), (b) and (c) shows the mean velocity gradient, Reynolds stress and turbulent production profiles for Case 1, 2 and 3. It is evident that when rheology is included in the simulation, the increased effective viscosity tends to reduce the velocity gradient near the wall. Since velocity gradient is the main driving force of turbulence, reduced velocity gradient also leads to reduced Reynolds stress and turbulent production. As can be seen in Figure 13 (c), turbulence production in Case 3 is suppressed by almost one order of magnitude due to enhanced viscosity .

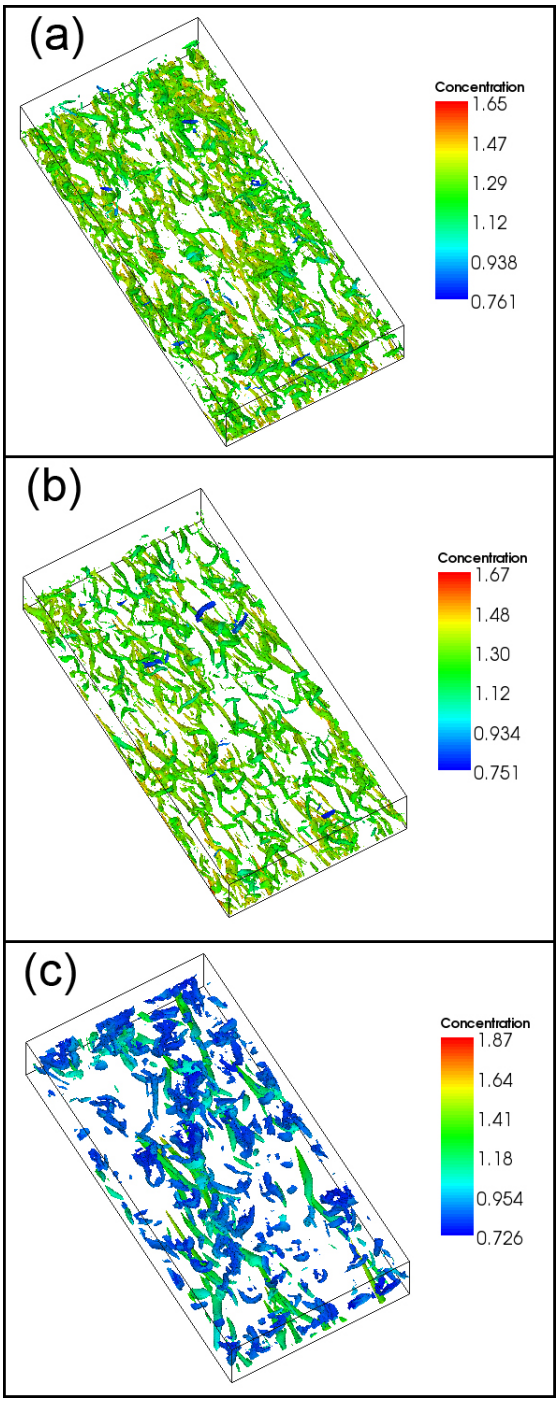

Figure 12: Turbulent coherent structures (a) Case 1 (without rheology), (b) Case 2 with Krieger-Dougherty rheology model with $\phi_m = 0.244$ and (c) Case 3 with Krieger-Dougherty rheology model with $\phi_m = 0.122$. The coherent structures are identified with λ_{ci} method with $\lambda_{ci} = 15$ for (a) and (b) and 5 for (c). The iso-surface is colored by sediment concentration.

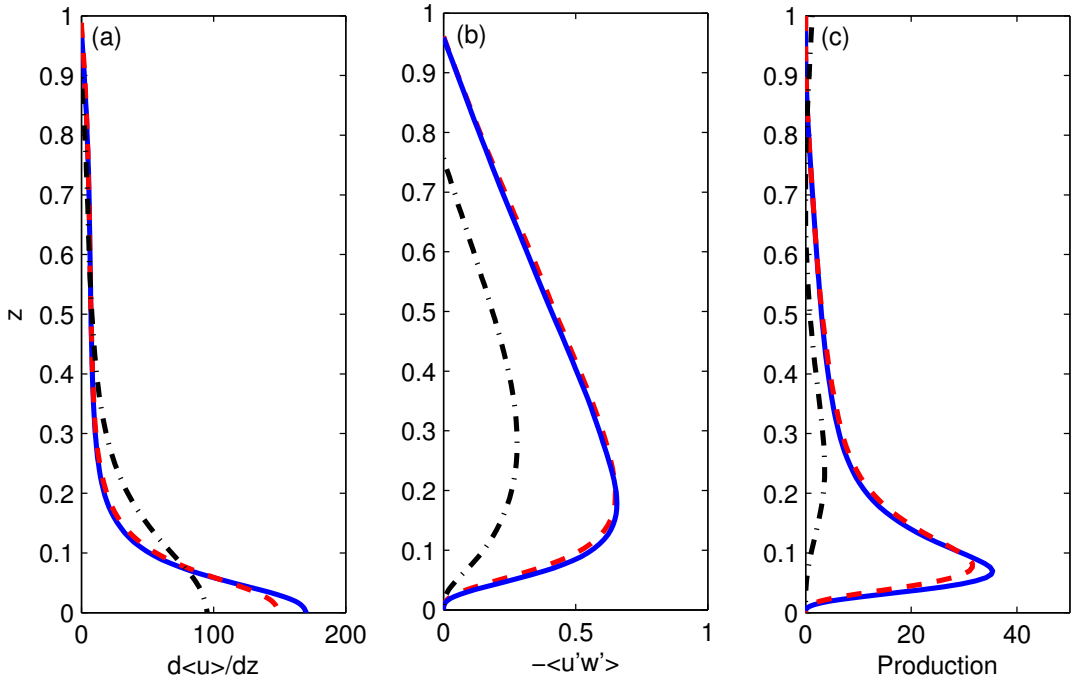

Figure 13: (a) Mean velocity gradient. (b) Reynolds stress profiles, (c) Turbulent Production, solid line represents model results for simulation without rheology model, dash line represents results from simulation with $\phi_m = 0.244$ and dash-solid line with $\phi_m = 0.122$.

5 Conclusion

To study fine sediment transport in turbulent boundary layers, a high accuracy turbulence-resolving numerical model that utilizes Fourier expansion in the streamwise and spanwise directions and sixth-order compact finite difference scheme in the wall-normal direction on Chebyshev grid points is developed. This hybrid scheme allows easy implementation of flow-dependent properties, such as viscosity, diffusivity and settling velocity while still maintain spectral-like numerical accuracy, critical for a turbulence-resolving model. The numerical model is validated with analytical solution for simple Newtonian rheology closure in laminar condition. To demonstrate the turbulence-resolving capability, the numerical model is further validated/verified with prior laboratory data and DNS results of turbulent channl flow at Reynolds number $Re = 180$, defined by the half channel depth and friction velocity. With $128 \times 128 \times 193$ mesh points in the streamwise, spanwise and vertical directions, the present numerical model is able to reproduce the mean velocity and RMS velocity fluctuations obtained by earlier DNS study of Kim et al. [*Kim et al.*(1987)] with a psuedo-spectral scheme.

Previous study by Cantero et al. [*Cantero et al.*(2009)] investigated the turbulence modulation by sediment induced density stratification. For a fixed *Re*, they found that the flow is characterized by two parameters, Richardson number and the non-dimensional settling velocity of sediment. For the property of sediment given, a critical Richardson number can be found, beyond which the flow turbulence collapses and flow undergoes laminazation. Hence, we are motivated to carry out a prelminary investigation on the modulation of flow turbulence by the presence of sediment due to sediment-induced density stratification and enhanced viscosity due to Newtonian rheology at Reynolds number $Re = 180$, Richardson number $Ri = 11.43$, nondimensional settling velocity $W_s = 0.02$. A simple Newtonian rheology model developed by Krieger and Dougherty [*Krieger and Dougherty*(1959)] is implemented where the magnitude of enhanced viscosity can be adjusted via a maximum packing concentration, which is interpreted here

as gelling concentration for cohesive sediment. By introducing rheology model into the system, we found that flow turbulence is damped by the increased effective viscosity and flow laminarization can occur at Richardson number below the critical value.

The rheology model used in this study is simple and idealized. In reality, the mud behaves as Non-Newtonian fluid and are often modeled as Bingham plastic fluid. In the near future, the more realistic rheology model will be used to study the effect of rheology on turbulence modulation. Also, we would like to apply this model to study the fine sediment transport in wave boundary layer to investigate the effect of rheological stress on turbulence modulation in the oscillatory bottom boundary layer.

A Appendix

A.1 Interpolation polynomials

For a given set of distinct points $x_i \in I$ and numbers u_i, the lagrange polynomial is the polynomial with least degree such that $u(x_i) = u_i$. The interpolation polynomial is just a linear combination of the Langrange basis polynomials on the given set I

$$u(x) = \sum_{j \in I}^{k} u_j l_j(x) \tag{53}$$

with the Lagrange basis polynomials specified as

$$l_i = \frac{\Pi_{j \in I \neq i}(x - x_j)}{\Pi_{j \in I \neq i}(x_i - x_j)} \tag{54}$$

with the operator of the product of a sequence defined as

$$\Pi(x) = \Pi_{j \in I}(x - x_j) \tag{55}$$

A.2 First derivative

A 6th order centered compact finite difference scheme on non-uniform grid is implemented in this study. The general form of compact scheme for the first derivative can by given as [*Shukla and Zhong*(2005)]

$$u_i' + \sum_{j \in I_n} a_j u_j' = b_i u_i + \sum_{j \in I_m \neq i} b_j u_j + \sum_{j \in I_n} c_j u_j \tag{56}$$

with the coefficients given as

$$b_i = l_i^{m'}(x_i) + 2\frac{\Pi_n'(x_i)}{\Pi_n(x_i)} \tag{57}$$

$$b_j = \left\{\frac{\Pi_n(x_i)}{\Pi_n(x_j)}\right\}^2 l_j^{m'}(x_i) \tag{58}$$

$$a_j = \frac{(x_j - x_i)\Pi_m'(x_i)}{\Pi_m(x_j)}\{l_j^n(x_i)\}^2 \tag{59}$$

$$c_j = \frac{\Pi_m'(x_i)}{\Pi_m(x_j)}\{l_j^n(x_i)\}^2\left[1 - \left\{2l_j^{n'}(x_j) + \frac{\Pi_m'(x_j)}{\Pi_m(x_j)}\right\}(x_i - x_j)\right] \tag{60}$$

with m and n representing the point set I_m and I_n respectively.

$$a_{i-1}u_{i-1}' + u_i' + a_{i+1}u_{i+1}' = b_{i-2}u_{i-2} + b_{i-1}u_{i-1} + b_iu_i + b_{i+1}u_{i+1} + b_{i+2}u_{i+2} \tag{61}$$

For the interior domain, the point sets can be given $I_m = \{i-2, i, i+2\}$ and $I_n = \{i-1, i+1\}$, the coefficients can be given as

$$a_{i-1} = \frac{(x_i - x_{i-2})(x_i - x_{i+2})(x_i - x_{i+1})^2}{(x_{i-1} - x_{i-2})(x_{i-1} - x_{i+2})(x_{i-1} - x_{i+1})^2} \tag{62}$$

$$a_{i+1} = \frac{(x_i - x_{i-2})(x_i - x_{i+2})(x_i - x_{i-1})^2}{(x_{i+1} - x_{i-2})(x_{i+1} - x_{i+2})(x_{i+1} - x_{i-1})^2} \tag{63}$$

$$b_{i-2} = \frac{(x_i - x_{i-1})^2(x_i - x_{i+1})^2(x_i - x_{i+2})}{(x_{i-2} - x_{i-1})^2(x_{i-2} - x_{i+1})^2(x_{i-2} - x_i)(x_{i-2} - x_{i+2})} \tag{64}$$

$$b_{i+2} = \frac{(x_i - x_{i-1})^2(x_i - x_{i+1})^2(x_i - x_{i-2})}{(x_{i+2} - x_{i-1})^2(x_{i+2} - x_{i+1})^2(x_{i+2} - x_i)(x_{i+2} - x_{i-2})} \tag{65}$$

$$b_i = \frac{1}{x_i - x_{i+2}} + \frac{1}{x_i - x_{i-2}} + \frac{2}{x_i - x_{i-1}} + \frac{2}{x_i - x_{i+1}} \tag{66}$$

$$\begin{aligned} c_{i-1} =& \frac{(x_i - x_{i-2})(x_i - x_{i+2})(x_i - x_{i+1})^2}{(x_{i-1} - x_{i-2})(x_{i-1} - x_{i+2})(x_{i-1} - x_i)(x_{i-1} - x_{i+1})^2} \\ & \left(2 - 2\frac{x_i - x_{i-1}}{x_{i-1} - x_{i+1}} - \frac{x_i - x_{i-1}}{x_{i-1} - x_{i-2}} - \frac{x_i - x_{i-1}}{x_{i-1} - x_{i+2}}\right) \end{aligned} \tag{67}$$

$$\begin{aligned} c_{i+1} =& \frac{(x_i - x_{i-2})(x_i - x_{i+2})(x_i - x_{i-1})^2}{(x_{i+1} - x_{i-2})(x_{i+1} - x_{i+2})(x_{i+1} - x_i)(x_{i+1} - x_{i-1})^2} \\ & \left(2 - 2\frac{x_i - x_{i+1}}{x_{i+1} - x_{i-1}} - \frac{x_i - x_{i+1}}{x_{i+1} - x_{i-2}} - \frac{x_i - x_{i+1}}{x_{i+1} - x_{i+2}}\right) \end{aligned} \tag{68}$$

A.3 Second derivative

The general form of the second order derivative can be written as

$$u_i'' + \sum_{j\in I_n} a_j u_j'' = b_i u_i + \sum_{j\in I_m \neq i} b_j u_j + \sum_{j\in I_n} c_j u_j \tag{69}$$

with the coefficients given as

$$\begin{aligned}
a_j &= -\Big\{\frac{\Pi_m''(x_i)}{\Pi_m(x_j)} l_j^n(x_i) + \frac{2\Pi_m'(x_i)}{\Pi_m(x_j)} l_j^{n\prime}(x_i)\Big\} \sum_{r=1}^{n} B_r (x_i - x_j)^r - \frac{2\Pi_m'(x_i)}{\Pi_m(x_j)} l_j^n(x_i) \sum_{r=1}^{n} r B_r (x_i - x_j)^{r-1} \\
b_j &= \Big\{\frac{\Pi_m''(x_i)}{\Pi_m(x_j)} l_j^n(x_i) + \frac{2\Pi_m'(x_i)}{\Pi_m(x_j)} l_j^{n\prime}(x_i)\Big\}[1 + \sum_{r=1}^{n} A_r (x_i - x_j)^r] + \frac{2\Pi_m'(x_i)}{\Pi_m(x_j)} l_j^n(x_i) \sum_{r=1}^{n} r A_r (x_i - x_j)^{r-1} \\
b_i &= \frac{\Pi_n''(x_i)}{\Pi_n(x_i)} + l_i^{m\prime\prime}(x_i) + 2C_2 + 2\frac{\Pi_n'(x_i)}{\Pi_n(x_i)} l_i^{m\prime}(x_i) + 2C_1\Big\{l_i^{m\prime}(x_i) + \frac{\Pi_n'(x_i)}{\Pi_n(x_i)}\Big\} \\
c_j &= \Big\{\frac{\Pi_n(x_i)}{\Pi_n(x_j)} l_j^{m\prime\prime}(x_i) + \frac{2\Pi_n(x_i)}{\Pi_n(x_j)} l_j^{m\prime}(x_i)\Big\}[1 + \sum_{r=1}^{n} C_r (x_i - x_j)^r] + \frac{2\Pi_n(x_i)}{\Pi_n(x_j)} l_j^{m\prime}(x_i) \sum_{r=1}^{n} r C_r (x_i - x_j)^{r-1}
\end{aligned}$$

with A_r given as

$$\begin{aligned}
&2A_2 + 2A_1\Big\{\frac{\Pi_m(x) l_i^n(x)}{\Pi_m(x_i)}\Big\}'\Big|_{x=x_i} + \Big\{\frac{\Pi_m(x) l_i^n(x)}{\Pi_m(x_i)}\Big\}''\Big|_{x=x_i} = 0, \quad j = i, \\
&\sum_{r=1}^{n} A_r \Big[(x_j - x_i)^r \Big\{\frac{\Pi_m(x) l_i^n(x)}{\Pi_m(x_i)}\Big\}''\Big|_{x=x_j} + 2r(x_j - x_i)^{r-1}\Big\{\frac{\Pi_m(x) l_i^n(x)}{\Pi_m(x_i)}\Big\}'\Big|_{x=x_j}\Big] + \Big\{\frac{\Pi_m(x) l_i^n(x)}{\Pi_m(x_i)}\Big\}''\Big|_{x=x_j} = 0, \quad \forall j \in I_n, i \in I_n, j \neq i
\end{aligned}$$

B_r given as

$$\begin{aligned}
&2B_2 + 2B_1\Big\{\frac{\Pi_m(x) l_i^n(x)}{\Pi_m(x_i)}\Big\}'\Big|_{x=x_i} = 1, \quad j = i, \\
&\sum_{r=1}^{n} B_r \Big[(x_j - x_i)^r \Big\{\frac{\Pi_m(x) l_i^n(x)}{\Pi_m(x_i)}\Big\}''\Big|_{x=x_j} + 2r(x_j - x_i)^{r-1}\Big\{\frac{\Pi_m(x) l_i^n(x)}{\Pi_m(x_i)}\Big\}'\Big|_{x=x_j}\Big] = 0, \quad \forall j \in I_n, i \in I_n \text{and} j \neq i
\end{aligned}$$

and C_r given as

$$\sum_{r=1}^{n} C_r \Big[(x_j - x_i)^r \Big\{\frac{\Pi_n(x) l_i^m(x)}{\Pi_n(x_i)}\Big\}''\Big|_{x=x_j} + 2r(x_j - x_i)^{r-1}\Big\{\frac{\Pi_n(x) l_i^m(x)}{\Pi_n(x_i)}\Big\}'\Big|_{x=x_j}\Big] + \Big\{\frac{\Pi_n(x) l_i^m(x)}{\Pi_n(x_i)}\Big\}''\Big|_{x=x_j} = 0 \quad j \in I_n, i \in I_m$$

In the interior domain, the 6th order centered compact finite difference scheme for the second derivative is

$$c_{i-1} u_{i-1}'' + u_i'' + c_{i+1} u_{i+1}'' = d_{i-2} u_{i-2} + d_{i-1} u_{i-1} + d_i u_i + d_{i+1} u_{i+1} + d_{i+2} u_{i+2} \tag{70}$$

Define

$$\begin{aligned}
D_1^+ &= \frac{1}{x_{i+1} - x_{i-2}} + \frac{1}{x_{i+1} - x_i} + \frac{1}{x_{i+1} - x_{i+2}} \\
D_1^- &= \frac{1}{x_{i-1} - x_{i-2}} + \frac{1}{x_{i-1} - x_i} + \frac{1}{x_{i-1} - x_{i+2}} \\
D_2^+ &= \frac{2}{(x_{i+1} - x_{i-2})(x_{i+1} - x_i)} + \frac{2}{(x_{i+1} - x_i)(x_{i+1} - x_{i+2})} + \frac{2}{(x_{i+1} - x_{i-2})(x_{i+1} - x_{i+2})} \\
D_2^- &= \frac{2}{(x_{i-1} - x_{i-2})(x_{i-1} - x_i)} + \frac{2}{(x_{i-1} - x_i)(x_{i-1} - x_{i+2})} + \frac{2}{(x_{i-1} - x_{i-2})(x_{i-1} - x_{i+2})}
\end{aligned}$$

and

$$
\begin{aligned}
D &= 6 + 4(x_{i+1} - x_{i-1})(D_1^+ - D_1^-) - 2(x_{i+1} - x_{i-1})^2 D_1^+ D_1^- \\
A_1^+ D &= -4D_1^+ - 2D_1^- + 2(x_{i+1} - x_{i-1})(D_1^+ D_1^- - D_2^+) + (x_{i+1} - x_{i-1})^2 D_2^+ D_1^- \\
A_1^- D &= -4D_1^- - 2D_1^+ + 2(x_{i-1} - x_{i+1})(D_1^+ D_1^- - D_2^-) + (x_{i-1} - x_{i+1})^2 D_2^- D_1^+ \\
A_2^+ D &= 4D_1^+ D_1^- - D_2^+ - \frac{2}{x_{i+1} - x_{i-1}}(D_1^+ - D_1^-) + (x_{i+1} - x_{i-1}) D_2^+ D_1^- \\
A_2^- D &= 4D_1^+ D_1^- - D_2^- - \frac{2}{x_{i-1} - x_{i+1}}(D_1^- - D_1^+) + (x_{i-1} - x_{i+1}) D_2^- D_1^+ \\
B_1^+ D &= -\Big\{ \frac{2}{x_{i-1} - x_{i+1}} + D_1^- \Big\}(x_{i-1} - x_{i+1})^2 \\
B_1^- D &= -\Big\{ \frac{2}{x_{i+1} - x_{i-1}} + D_1^+ \Big\}(x_{i-1} - x_{i+1})^2 \\
B_2^+ D &= 1 - (x_{i+1} - x_{i-1}) D_1^- \\
B_2^- D &= 1 - (x_{i-1} - x_{i+1}) D_1^+
\end{aligned}
$$

for C_{1j} and C_{2j} with $j \in \{i-2, i, i+2\}$

$$
\begin{aligned}
C_{1j} D = {} & \frac{x_{i+1} + x_{i-1} - 2x_j}{(x_{i+1} - x_j)(x_{i-1} - x_j)} \Big\{ 10 + \frac{4(x_{i+1} - x_{i-1})^2}{(x_{i+1} - x_j)(x_{i-1} - x_j)} \Big\} \\
& + 2(x_{i+1} - x_{i-1}) \Big\{ \frac{x_{i+1} - x_j}{x_{i-1} - x_j} - \frac{x_{i-1} - x_j}{x_{i+1} - x_j} \Big\} D_1^+ D_1^- \\
& + D_1^- \Big\{ \frac{4(x_{i+1} - x_{i-1})}{x_{i-1} - x_j} + \frac{4(x_{i+1} - x_{i-1})}{x_{i+1} - x_j} - \frac{2(x_{i+1} - x_{i-1})^2}{(x_{i+1} - x_j)^2} \Big\} \\
& - D_1^+ \Big\{ \frac{4(x_{i+1} - x_{i-1})}{x_{i-1} - x_j} + \frac{4(x_{i+1} - x_{i-1})}{x_{i+1} - x_j} + \frac{2(x_{i+1} - x_{i-1})^2}{(x_{i+1} - x_j)^2} \Big\}
\end{aligned}
$$

$$
\begin{aligned}
C_{2j} D = {} & 2 \Big\{ \frac{1}{(x_{i+1} - x_j)^2} + \frac{1}{(x_{i-1} - x_j)^2} + \frac{1}{(x_{i-1} - x_j)(x_{i+1} - x_j)} \Big\} - \frac{2(x_{i+1} - x_{i-1})^2}{(x_{i-1} - x_j)(x_{i+1} - x_j)} D_1^+ D_1^- \\
& - 2D_1^+ \frac{x_{i-1} - x_{i+1}}{x_{i-1} - x_j} \Big\{ \frac{1}{x_{i-1} - x_j} + \frac{1}{x_{i+1} - x_j} \Big\} - 2D_1^- \frac{x_{i+1} - x_{i-1}}{x_{i+1} - x_j} \Big\{ \frac{1}{x_{i-1} - x_j} + \frac{1}{x_{i+1} - x_j} \Big\}
\end{aligned}
$$

with the coefficients given as

$$
\begin{aligned}
c_{i-1} = {} & 2(x_i - x_{i-2})(x_i - x_{i+2})[B_1^-(2x_i - x_{i+1} - x_{i-1}) + B_2^-(3x_i - 2x_{i+1} - x_{i-1})] \\
& + 2(2x_i - x_{i-2} - x_{i+2})(x_i - x_{i+1})(x_i - x_{i-1})[B_1^- + (x - x_{i-1})B_2^-] \\
& / (x_{i+1} - x_{i-1})(x_{i-1} - x_{i-2})(x_{i-1} - x_i)(x_{i-1} - x_{i+2})
\end{aligned} \tag{71}
$$

$$
\begin{aligned}
c_{i+1} = {} & 2(x_i - x_{i-2})(x_i - x_{i+2})[B_1^+(2x_i - x_{i+1} - x_{i-1}) + B_2^+(3x_i - 2x_{i-1} - x_{i+1})] \\
& + 2(2x_i - x_{i-2} - x_{i+2})(x_i - x_{i+1})(x_i - x_{i-1})[B_1^+ + (x - x_{i+1})B_2^+] \\
& / (x_{i+1} - x_{i-1})(x_{i+1} - x_{i-2})(x_{i+1} - x_i)(x_{i+1} - x_{i+2})
\end{aligned} \tag{72}
$$

$$
\begin{aligned}
d_{i-2} = {} & \frac{2(x_i - x_{i-1})(x_i - x_{i+1})(x_i - x_{i+2})}{(x_{i-2} - x_{i+1})(x_{i-2} - x_{i-1})(x_{i-2} - x_{i+2})(x_{i-2} - x_i)} \Big\{ C_{12}^- \Big(1 + \frac{x_i - x_{i-2}}{x_i - x_{i+1}} + \frac{x_i - x_{i-2}}{x_i - x_{i-1}} \Big) \\
& + C_{22}^- \Big(2 + \frac{x_i - x_{i-2}}{x_i - x_{i+1}} + \frac{x_i - x_{i-2}}{x_i - x_{i-1}} \Big)(x_i - x_{i-2}) + \frac{1}{x_i - x_{i+1}} + \frac{1}{x_i - x_{i-1}} \Big\} \\
& + \frac{2(x_i - x_{i+1})(x_i - x_{i-1})}{(x_{i-2} - x_{i+1})(x_{i-2} - x_{i-1})(x_{i-2} - x_i)(x_{i-2} - x_{i+2})} [1 + C_{12}^-(x_i - x_{i-2}) + C_{22}^-(x_i - x_{i-2})^2]
\end{aligned} \tag{73}
$$

$$
\begin{aligned}
d_{i-1} = {} & 2(x_i - x_{i-2})(x_i - x_{i+2})[1 + A_1^-(2x_i - x_{i+1} - x_{i-1}) + A_2^-(x_i - x_{i-1})(3x_i - 2x_{i+1} - x_{i-1})] \\
& + 2(2x_i - x_{i-2} - x_{i+2})[1 + A_1^-(x_i - x_{i-1}) + A_2^-(x_i - x_{i-1})^2] \\
& / (x_{i-1} - x_{i+1})(x_{i-1} - x_{i-2})(x_{i-1} - x_i)(x_{i-1} - x_{i+2})
\end{aligned} \tag{74}
$$

$$
\begin{aligned}
d_i = {} & 2C_{2i} + 2C_{1i}\Big\{\frac{2x_i - x_{i-1} - x_{i+1}}{(x_i - x_{i+1})(x_i - x_{i-1})} + \frac{2x_i - x_{i-2} - x_{i+2}}{(x_i - x_{i-2})(x_i - x_{i+2})}\Big\} \\
& + \frac{2 + 2(2x_i - x_{i+1} - x_{i-1})(2x_i - x_{i-2} - x_{i+2})/(x_i - x_{i-2})(x_i - x_{i+2})}{(x_i - x_{i+1})(x_i - x_{i-1})} \\
& + \frac{2}{(x_i - x_{i-2})(x_i - x_{i+2})}
\end{aligned} \tag{75}
$$

$$
\begin{aligned}
d_{i+1} = {} & 2(x_i - x_{i-2})(x_i - x_{i+2})[1 + A_1^+(2x_i - x_{i+1} - x_{i-1}) + A_2^+(x_i - x_{i+1})(3x_i - 2x_{i-1} - x_{i+1})] \\
& + 2(2x_i - x_{i-2} - x_{i+2})[1 + A_1^+(x_i - x_{i+1}) + A_2^+(x_i - x_{i+1})^2] \\
& /(x_{i+1} - x_{i-1})(x_{i+1} - x_{i-2})(x_{i+1} - x_i)(x_{i+1} - x_{i+2})
\end{aligned} \tag{76}
$$

$$
\begin{aligned}
d_{i+2} = {} & \frac{2(x_i - x_{i-1})(x_i - x_{i+1})(x_i - x_{i-2})}{(x_{i+2} - x_{i+1})(x_{i+2} - x_{i-1})(x_{i+2} - x_{i-2})(x_{i+2} - x_i)}\Big\{C_{12}^+\Big(1 + \frac{x_i - x_{i+2}}{x_i - x_{i+1}} + \frac{x_i - x_{i+2}}{x_i - x_{i-1}}\Big) \\
& + C_{22}^+\Big(2 + \frac{x_i - x_{i+2}}{x_i - x_{i+1}} + \frac{x_i - x_{i+2}}{x_i - x_{i-1}}\Big)(x_i - x_{i+2}) + \frac{1}{x_i - x_{i+1}} + \frac{1}{x_i - x_{i-1}}\Big\} \\
& + \frac{2(x_i - x_{i+1})(x_i - x_{i-1})}{(x_{i+2} - x_{i+1})(x_{i+2} - x_{i-1})(x_{i+2} - x_i)(x_{i+2} - x_{i-2})}[1 + C_{12}^+(x_i - x_{i+2}) + C_{22}^+(x_i - x_{i+2})^2]
\end{aligned} \tag{77}
$$

Reference

[*Acrivos et al.*(1993)] Acrivos, A., R. Mauri, and X. Fan (1993), Shear-induced resuspension in a couette device, *International Journal of Multiphase Flow*, *19*(5), 797–802.

[*Arakawa and Lamb*(1980)] Arakawa, A., and V. R. Lamb (1980), A potential enstrophy and energy conserving scheme for the shallow water equation, *Monthly weather review*, *109*, 18–36.

[*Balachandar and Eaton*(2010)] S. Balachandar and John K. Eaton (2010), Turbulent Dispersed Multiphase Flow, *Annual review of Fluid mechanics*, *42*, 111-133

[*Boersma*(2011)] Boersma, B. J. (2011), A 6th order staggered compact finite difference method for the incompressible navier-stokes and scalar transport equations, *Journal of Computational Physics*, *230*, 4940–4954.

[*Boyd*(2001)] Boyd, J. P. (2001), *Chebyshev and Fourier spectral methods*, DOVER publication Inc.

[*Cantero et al.*(2009)] Cantero, M. I., S. Balachandar, A. Cantalli, C. Primez, and G. Parker (2009), Turbidity current with a roof: Direct numerical simulation of self-stratified turbulent channel flow driven by suspended sediment, *JGR*, *114*(C03008).

[*Cantero et al.*(2012)] Cantero, M. I., A. Cantalli, C. Pirmez, S. Balachandar, D. Mohrig, T. A. Hickson, T.-H. Yeh, H. Naruse, and G. Parker (2012), Emplacement of massive turbidities linked to extinction of turbulence in turbidity currents, *Nature Geoscience*, *5*, 42–45.

[*Canuto et al.*(2011)] Canuto, C. G., M. Y. Hussaini, A. Quarteroni, and T. A. Zang (2011), *Spectral Methods: Fundamentals in Single Domains*, Springer.

[*Chorin*(1968)] Chorin, A. J. (1968), Numerical solution of the navier-stokes equations, *Math. Comp.*, *22*, 745–762.

[*Colonius*(2004)] Colonius, T. (2004), Modeling artificial boundary conditions for compressible flow, *Annual review of Fluid mechanics*, *36*, 315–345.

[*Comte-Bellot*(1963)] Comte-Bellot, G. (1963), Contribution a l'ètude de la turbulence de conduite, Ph.D. thesis, University of Grenoble.

[*Cortese and Balachandar*(1995)] Cortese, T. A., and S. Balachandar (1995), High performance spectral simulation of turbulent flows in massively parallel machines with distributed memory, *The international journal of high performance computing applications*, *9*(3), 187–204.

[*Eckelmann*(1974)] Eckelmann, H. (1974), The structure of the viscous sublayer and the adjacent wall region in a turbulent channel flow, *Journal of Fluid mechanics*, *65*.

[*Engel and Schartau*(1999)] Engel, A. and Schartau, M. (1999), Influence of transparent expolymer particles (TEP) on sinking velocity of Nitzschia closterum aggregates, *Marine Ecology Progress Series*,*182*,69-76

[*Einstein*(1906)] Einstein (1906), Eine neue bestimmung der molekuldimensionen, *Ann. Physik.*, *19*, 289–306.

[*Ferry and Balachandar*(2001)] Balachandar, S. and Ferry, J. (2001) A fast Eulerian method for two-phase flow, *International Journal of Multiphase Flow*, *27*, 1199-1226.

[*Ferry and Balachadar*(2002)] Balachandar, S. and Ferry, J. (2002) Equilibrium expansion for the Eulerian velocity of small particles, *Powder Technol.*, *125*, 131-139.

[*Gottlieb and Orszag*(1987)] Gottlieb, D., and S. A. Orszag (1987), *Numerical analysis of spectral methods: Theory and Applications*, Society for Industrial and Applied Mathematics.

[*Hokpunna and Manhart*(2010)] Hokpunna, A., and M. Manhart (2010), Compact fourth-order finite volume method for numerical solutions of navier-stokes equations on staggered grids, *Journal of Computational Physics*, (7545-7570).

[*Hopfinger*(1987)] Hopfinger, E. J. (1987), Turbulence in stratified fluids: A review, *JGR*, *92*(C5), 5287–5303.

[*Kessel and Kranenburg*(1996)] Kessel, T., and C. Kranenburg (1996), Gravity current of fluid mud on sloping bed, *Journal of Hydraulic Engineering*, *122*(12), 710–717.

[*Kim et al.*(1987)] Kim, J., P. Moin, and R. Moser (1987), Turbulence statistics in fully developed channel flow at low reynolds number, *Journal of Fluid Mechanics*, *177*, 133–166.

[*Krieger*(1972)] Krieger, I. M. (1972), Rheology of monodisperse lattices, *Adv. Colloid Interface Sci.*, *3*, 111–136.

[*Krieger and Dougherty*(1959)] Krieger, I. M., and T. J. Dougherty (1959), A mechanism for non-newtonian flow in suspensions of rigid spheres, *Trans. Soc. Rheol.*, *3*, 137–152.

[*Leighton and Acrivos*(1986)] Leighton, D., and A. Acrivos (1986), Viscous resuspension, *Chemical Engineering Science*, *41*(6), 1377–1384.

[*Lele*(1992)] Lele, S. K. (1992), Compact finite difference schemes with spectral like resolution, *Journal of Computational Physics*, *103*, 16–42.

[*Liu and Mei*(1990)] Liu, K. F., and C. C. Mei (1990), Approximate equations for the slow spreading of a thin sheet of bingham plastic fluid, *Physics of Fluid A*, *2*(1), 30–36.

[*Moin and Kim*(1982)] Moin, P., and J. Kim (1982), Numerical investigation of turbulent channel flow, *Journal of Fluid mechanics*, *118*, 341–377.

[*Moser and Moin*(1987)] Moser, R. D., and P. Moin (1987), The effects of curvature in wall-bounded turbulent flows, *Journal of Fluid mechanics*, *175*, 479–510.

[*Ozdemire et al.*(2010)] Ozdemire, C. E., T.-J. Hsu, and S. Balachandar (2010), A numerical investigation of fine particle laden flow in an oscillatory channel: the role of particle-induced density stratification, *Journal of Fluid mechanics*, *665*, 1–45.

[*Pereira et al.*(2001)] Pereira, J. M. C., M. H. Kobayashi, and J. C. F. Pereira (2001), A fourth-order-accurate finite volume compact method for the incompressible navier-stokes solutions, *Journal of Computational Physics*, *167*, 217–243.

[*Sahin et al.*(2012)] Sahin, C., I. Safak, A. Sheremet, and A. J. Mehta (2012), Observations on cohesive bed reworking by waves: Atchafalaya shelf, louisiana, *JGR*, *117*(CO9025), 14.

[*Santschi et al.*(2005)] Santschi, P. H., A. B. Burd, J.-F. Gailard, and A. A. Lazarides (2005), Transport of materials and chemicals by nanoscale colloids and micro- to macro-scale flocs in marine, freshwater and engineered systems, in *Flocculation in natural and engineered environmental system*, edited by I. G. Droppo, G. G. Leppard, S. N. Liss, and T. G. Milligan, pp. 191–209, CRC Press.

[*Schaflinger et al.*(1990)] Schaflinger, U., A. Acrivos, and K. Zhang (1990), Viscous resuspension of a sediment within a laminar and stratified flow, *International Journal of Multiphase Flow*, *16*(4), 567–578.

[*Shah et al.*(2010)] Shah, A., L. Yuan, and A. Khan (2010), Upwind compact finite difference scheme for time-accurate solution of the incompressible navier-stokes equations, *Journal of Computational Physics*, *215*, 3201–3213.

[*Shukla and Zhong*(2005)] Shukla, R. K., and X. Zhong (2005), Derivation of high-order compact finite difference schemes for non-uniform grid using polynomial interpolation, *Journal of Computational Physics*, *204*, 404–429.

[*Shukla et al.*(2007)] Shukla, R. K., M. Tatineni, and X. Zhong (2007), Very high-order compact finite difference schemes on non-uniform grids for incompressible navier-stokes equations, *Journal of Computational Physics*, (1064-1094).

[*Spalart*(1988)] Spalart, P. R. (1988), Direct numerical simulation of a turbulent boundary layer up to re_θ=1410, *Journal of Fluid Mechanics*, *187*, 61–98.

[*Stickel and Powell*(2005)] Stickel, J. J., and R. L. Powell (2005), Fluid mechanics and rheology of dense suspensions, *Annual review of Fluid mechanics*, *37*, 129–149.

[*Teisson et al.*(1992)] Teisson, C., O. Simmonin, J. C. Galland, and D. Laurence (1992), Turbulent modelling and mud sedimentation: A reynolds stress model and a two-phase flow model, in *The 23rd International Conference on Coastal Engineering*.

[*Traykovski*(2010)] Traykovski, P. (2010), Observations of mechanisms of dissipation of wave energy over a muddy seabed, *Invited) Eos Trans. AGU*, *91*.

[*Wei and Willmarth*(1989)] Wei, T., and W. W. Willmarth (1989), Reynolds number effects on the structure of a turbulent channel flow, *Journal of Fluid mechanics*, *204*, 57–95.

[*Williamson*(1980)] Williamson, J. H. (1980), Low-storage runge-kutta schemes, *Journal of Computational Physics*, *35*, 48–56.

[*Winterwerp*(2001)] Winterwerp, J. C. (2001), Stratification effects by cohesive and noncohesive sediment, *JGR*, *106*(C10), 22,559–22,574.

[*Winterwerp*(2002)] Winterwerp, J. C. (2002), On flocculation and settling velocity of estuarine mud, *Cont. Shelf Res.*,*22*(9),1339-1360.

[*Zhong and Tatineni*(2003)] Zhong, X., and M. Tatineni (2003), High-order non-uniform grid schemes for numerical simulation of hypersonic boundary layer stability and transition, *Journal of Computational Physics*, *190*, 419–458.

[*Zhou and Ni*(1995)] Zhou, D., and J. R. Ni (1995), Effects of dynamics interaction on sediment laden turbulent flows, *JGR*, *100*(C1), 981–996.

[*Zhou et al.*(1999)] Zhou, J., R. J. Adrian, S. Balachandar, and T. M. Kendall (1999), Mechanisms for generating coherent packets of hairpin vortices in channel flow, *Journal of Fluid Mechanics*, *387*, 353–396.